



저작자표시-비영리-동일조건변경허락 2.0 대한민국

이용자는 아래의 조건을 따르는 경우에 한하여 자유롭게

- 이 저작물을 복제, 배포, 전송, 전시, 공연 및 방송할 수 있습니다.
- 이차적 저작물을 작성할 수 있습니다.

다음과 같은 조건을 따라야 합니다:



저작자표시. 귀하는 원저작자를 표시하여야 합니다.



비영리. 귀하는 이 저작물을 영리 목적으로 이용할 수 없습니다.



동일조건변경허락. 귀하가 이 저작물을 개작, 변형 또는 가공했을 경우에는, 이 저작물과 동일한 이용허락조건하에서만 배포할 수 있습니다.

- 귀하는, 이 저작물의 재이용이나 배포의 경우, 이 저작물에 적용된 이용허락조건을 명확하게 나타내어야 합니다.
- 저작권자로부터 별도의 허가를 받으면 이러한 조건들은 적용되지 않습니다.

저작권법에 따른 이용자의 권리는 위의 내용에 의하여 영향을 받지 않습니다.

이것은 [이용허락규약\(Legal Code\)](#)을 이해하기 쉽게 요약한 것입니다.

[Disclaimer](#)

ABSTRACT

Positron Emission Tomography Detectors Based on Silicon Photomultiplier

Sun Il Kwon
Interdisciplinary Program
In Radiation Applied Life Science
Seoul National University College of Medicine

Silicon photomultiplier (SiPM) is a promising semi-conductor photo-sensor in positron emission tomography (PET), simultaneous PET/MRI, and time-of-flight PET because it is intrinsically MR-compatible and has comparable internal gain and timing properties to a photomultiplier tube (PMT). Their compact size enables one-to-one coupling between the crystal and SiPM to yield the best timing performance. However, huge and complex electronics are required for operating each individual SiPM. The aim of this study was to investigate into the use of SiPM for PET and to develop small animal PET scanner and time-of-flight PET block detector.

The SiPM PET consists of 8 detectors, each of which is composed of 2×6 SiPMs and 4×13 LGSO crystals. Each crystal has dimensions of $1.5 \times 1.5 \times 7$ mm³. The crystal face-to-face diameter and axial FOV are 6.0 cm and 6.5 mm, respectively. Bias voltage is applied to each SiPM using a finely-controlled voltage supply because the gain of the SiPM strongly depends on the supply voltage. Reconstructed PET images using a maximum-likelihood expectation-maximization (MLEM) algorithm were co-registered with animal

X-ray CT images. All individual LGSO crystals within the detectors were clearly distinguishable in flood images obtained by irradiating the detector using a ^{22}Na point source. The energy resolution for individual crystals was $25.8 \pm 2.6\%$ on average for 511 keV photo-peaks. The spatial resolution measured with the ^{22}Na point source in a warm background was 1.0 mm (2 mm off center) and 1.4 mm (16 mm off center) when the MLEM algorithm was applied. A myocardial ^{18}F -FDG study in mice and a skeletal ^{18}F study in rats demonstrated the fine spatial resolution of the scanner. The feasibility of the SiPM PET was also confirmed in the tumor images of mice using ^{18}F -FDG and ^{68}Ga -RGD, and the brain images of rats using ^{18}F -FDG.

Proposed time-of-flight PET block detector using SiPM array are comprised of several $M \times N$ SiPM array blocks with signal encoding method and a field-programmable gate array (FPGA) board, which had developed digital time-to-digital converters (TDCs). Each SiPM was directly coupled with an LGSO crystal ($3 \times 3 \times 20 \text{ mm}^3$). Each output signal of SiPM is connected to each row and column that reduces the output signals from $M \times N$ to $M + N$. These row and column signals were used to measure energy and timing information of each incident γ -ray event, respectively. To verify the signal encoding methods for TOF PET block detector, various sizes of SiPM array (4×4 , 8×8 , and 12×12) were tested using standard methods for energy and time measurement. In the front-end electronics board for 4×4 SiPM array, comparators were used to convert row and column signals from analog to digital signals. These converted row and column digital signals transferred to a FPGA board. In FPGA, these row and column signals were

used to measured energy and time information only using developed digital TDCs. Time-over-threshold (TOT) method was used to measure energy using time duration without traditional energy measurement method. By applying signal encoding method, coincidence timing resolution slightly increased in large array, but the resolutions from the 12×12 SiPM array showed sufficient results for the use of TOF PET scanners. The developed digital TDCs on FPGA had the least square bit of ~ 15 ps. The intrinsic timing resolutions of ~ 130 ps were measured using developed TDC and two front-end boards without SiPMs. Dependence of TOT value on γ -ray energy was obtained with various radiation sources and the results showed clearly distinguishable. Coincidence γ -ray measurements were performed using ^{22}Na . The coincidence timing resolution of ~ 450 ps was obtained, which was comparable with conventional TOF PET scanners.

In conclusion, these results indicate that it is possible to develop a PET using a promising semi-conductor photo-sensor, which yielded reasonable PET performances in phantom and animal studies. Moreover, proposed time-of-flight PET detector can enable the development of a simple and cost-effective block detector for human time-of-flight PET scanner without traditional energy measurement method and individual SiPM readout in the block detector.

Keywords: PET, silicon photomultiplier (SiPM), PET/MR, time-of-flight PET, time-over-threshold, time-to-digital convertor

Student number: 2007-22070

CONTENTS

Abstract in English	i
Contents	iv
List of figures	v
List of tables	ix
List of abbreviations	x
General Introduction	2
Chapter 1	4
Small animal PET	
Introduction	5
Material and Methods	7
Results	24
Discussion	40
Conclusion	45
Chapter 2	46
Time-of-Flight PET Block Detector	
Introduction	47
Material and Methods	50
Results	65
Discussion	85
Conclusion	90
General Conclusion	91
References	92
Abstract in Korean	101

LIST OF FIGURES

Figure 1.1	Crystal block dimension of a detector module	11
Figure 1.2	(a) Circuit diagram of position-encoding board. (b) Assembly of the LGSO/SiPM detector block, pre-amplifier, and position-encoding boards.	14
Figure 1.3	Configuration of a prototype SiPM PET camera	16
Figure 1.4	Schematic of the assembly of the detector modules	17
Figure 1.5	Basic characteristics of SiPM used in this study. QDC output values from one of the stable (a) and unstable (b) SiPMs as a function of time in the LED test. (c) Wide distribution of optimal bias voltage to obtain the same level of QDC output. (d) Dependence of QDC output from SiPM on bias voltage. The straight line is a linear fit of data.	25
Figure 1.6	Intrinsic properties of detector module. (a) Flood map acquired using a LGSO/SiPM detector module. (b) Energy spectra of all 52 crystals in this module.	27
Figure 1.7	Physical performance of SiPM PET camera. (a) Sensitivity values measured at various axial offset (circle: 250-750 keV energy window; square: 350-650 keV; triangle: 400-600 keV). (b) Spatial resolution values measured at various radial offset (circle: tangential; square: radial).	29
Figure 1.8	Image of Ultra-Micro Phantom with 6 hollow channels (a). The lines indicate the position of the profile shown in (b).	32

Figure 1.9	Image of a uniform cylinder phantom	33
Figure 1.10	Tumor imaging in mice. (a) ^{18}F -FDG PET study in a mouse bearing a colon carcinoma. (b) ^{68}Ga -RGD PET study in a mouse bearing a malignant glioma cell line.	34
Figure 1.11	The coronal and sagittal views (fusion images) of ^{18}F -FDG PET of a mouse bearing a colon carcinoma.....	35
Figure 1.12	Short axis images of ^{18}F -FDG myocardial PET acquired without electrocardiogram gating in a mouse. The line on 4 th plane indicates the position of the profile shown in Figure 1.13	36
Figure 1.13	Profile of the ^{18}F -FDG myocardial PET image in a mouse.	37
Figure 1.14	PET images of rats. (a) ^{18}F bone PET study in a rat head region. (b) ^{18}F -FDG PET study in a rat brain.	38
Figure 1.15	^{18}F bone PET images acquired in the same rat using the developed SiPM based scanner (a) and a PMT-based GE eXplore VISTA scanner (b).	39
Figure 2.1	Conceptual diagram of the proposed signal encoding method. Output signals from the SiPM channels are tied together in row and column lines. The row and column signals are used to measure the energy and timing information of each incident γ -ray event, respectively.	52
Figure 2.2	Front-end electronics circuit board implemented for testing of the proposed signal encoding method (a), the LGSO crystal array (b), and dimension of a crystal frame (c).	55

Figure 2.3	Test setup for performance measurement of the developed detector block and the signal encoding method.	58
Figure 2.4	4×4 LGSO crystal ($3 \times 3 \times 20 \text{ mm}^3$) array and crystal holding frame (a) and proposed block detector – front-end board with crystal frame (b).	60
Figure 2.5	Test setup to measure coincidence γ -ray events	64
Figure 2.6	Energy spectra for a single SiPM device, which consists of 4×4 SiPM channels.	67
Figure 2.7	Photo-peak positions of the energy spectra as functions of bias voltage for a typical SiPM device. The plots fitted well with a second-order polynomial curve. The breakdown voltage was defined as the zero-crossing point of a fitted curve.....	68
Figure 2.8	Breakdown voltage distribution of each channel in all 12×12 SiPM arrays. The SiPM channels in each of the SiPM devices (packaged by a solid line) showed uniform breakdown voltage distributions (unit of color bar: [V]).	69
Figure 2.9	Coincidence time resolutions for one SiPM channel from each device as a function of overvoltage under different LED thresholds.....	70
Figure 2.10	Distribution of the coincidence time resolutions of nine 4×4 SiPM arrays (a), an 8×8 SiPM array (b), and a 12×12 SiPM array (c); the average coincidence time resolutions were 311 ps, 320 ps, and 335 ps, respectively. The blue dashed box indicates the SiPM devices used in the 8×8 SiPM.....	73

Figure 2.11	Distribution of the energy resolutions of nine 4×4 SiPM arrays (a), an 8×8 SiPM array (b), and a 12×12 SiPM array (c); the average coincidence time resolutions were 11.8%, 12.5%, and 12.8%, respectively. The blue dashed box indicates the SiPM devices used in the 8×8 SiPM array.	75
Figure 2.12	Propagation delay along the SiPM channels in a typical SiPM device. The SiPM channel number 13 was the closest channel to the input pin of the amplifier.....	77
Figure 2.13	Simulation result after place and route of one channel fine counter module delay look-up-table (circle: simulated TDC delayed time, straight line: linear fit, ~ 15 ps/bin slope).	79
Figure 2.14	Dependences of TOT value and TOT resolution on γ -ray energy obtained with a variety of radiation sources (131I: 362 keV, 22Na: 511 keV, 137Cs: 662 keV). The diamond and square represent TOT peak position and TOT resolution, respectively.	81
Figure 2.15	Time difference distributions of between two proposed detectors and a digital TDC on FPGA. The timing resolution between two detectors was ~ 130 ps.	82
Figure 2.16	Coincidence γ -ray measurements using ^{22}Na point source and two proposed detectors; TOT value (a) and time difference (b) distributions.	84

LIST OF TABLES

Table 2.1	Average breakdown voltage and +2.2 V overvoltage for each SiPM device, which was supplied to the circuit board developed for the performance measurements.....	71
Table 2.2	Measured average coincidence time resolution between SiPM detectors and reference PMT detector, and calculated single and coincidence time resolutions of SiPM detectors. Single time resolution of the reference PMT detector was 200 ps.....	74

LIST OF ABBREVIATIONS

<i>Full Name</i>	<i>Abbreviations</i>
Analog to Digital Convertor	ADC
Charge to Digital Convertor	QDC
Computed Tomography	CT
Full Width at Half Maximum	FWHM
Leading Edge Discriminator	LED
Magnetic Resonance Imaging	MRI
Maximum-Likelihood Expectation-Maximization	MLEM
Nuclear Instrumentation Module	NIM
Photomultiplier Tube	PMT
Positron Emission Tomography	PET
Silicon Photomultiplier	SiPM
Time of Flight	TOF
Time over Threshold	TOT
Time to Digital Convertor	TDC
Versa Module Europa	VME

GENERAL INTRODUCTION

Nuclear medicine imaging systems are widely used for non-invasive evaluation of functional and molecular abnormalities in living body. These imaging systems enable the quantitative assessment of in vivo distribution of radiopharmaceuticals. Two types of tomographic imaging devices are currently used in clinical nuclear medicine. One of them is single photon emission computed tomography (SPECT) using gamma camera that detects single γ -ray photons emitted from single photon emitters. The other one is positron emission tomography (PET) that detects a pair of γ -rays mutually annihilated from the positron emitters.

In particular, PET is commonly used to diagnose cancer or brain diseases using positron emitting radiopharmaceuticals. Most of the commercial PET systems employ scintillation detectors in which the visible photons generated from scintillation crystals are detected by photo-sensors. The most common photo-sensor used in PET is a photomultiplier tube (PMT). This device has several advantages, including excellent signal amplification gain ($\sim 10^6$) and stable operating properties against adverse environmental factors, such as temperature change. However, its bulk size and sensitivity to an external magnetic field are the major disadvantages of the PMT particularly in the combination of PET with magnetic resonance imaging (MRI) system (1,2). Meanwhile, various semi-conductor photo-sensors have been developed. Especially, silicon photomultiplier (SiPM; also called a

Geiger-mode APD [G-APD]) is in the spotlight as the key player in the next generation PET systems.

The aim of this thesis was to develop SiPM-based scintillation detectors which are suitable for high resolution small animal PET and MR-compatible time-of-flight PET scanners. In Chapter 1, a small animal PET scanner was developed using SiPMs. The basic properties of SiPM were investigated and block detector that consisted of LGSO crystal and SiPM arrays was developed. The performance of PET scanner built with these detector modules and results of phantom and animal studies will be presented. In Chapter 2, time-of-flight PET detector block was developed also using SiPM. A novel signal encoding method to reduce the complexity of signal readout and processing electronics and to adopt optimized signal amplifier stages for energy and timing measurements will be presented. Compact digital electronics developed for energy and timing measurement using field-programmable gate array (FPGA) was combined with the signal encoding method.

CHAPTER 1

Small Animal PET

INTRODUCTION

Compared to the PMT, the avalanche photodiode (APD; a semi-conductor photo-sensor), has a relatively compact size and is insensitive to magnetic fields. Because of these advantages, the APD is increasingly used in high-resolution PET detectors for small animal or organ-specific imaging (3-5), and in the development of combined PET/MRI systems (6-9). Although the APD is a mature and established technique in PET detector development, low internal gain (10^2 - 10^3) and slow signal output are the known limitations of this device (2,10,11).

SiPM is a promising alternative semi-conductor photo-sensor in PET and PET/MRI systems because it is insensitive to magnetic fields, has comparable internal gain and timing properties to the PMT, and compact size (10-12). The SiPM is an array of APD micro-cells operated in the Geiger mode and connected in parallel to a common output. Thus, the output pulse amplitude of the SiPM is proportional to the number of light photons emitted by the scintillation crystal, which interact with the micro-cells (13,14). Good linearity between the pulse amplitude and incident γ -ray energy can therefore be achieved if the number of light photons yielded from the crystal is proportional to the γ -ray energy, and the number of micro-cells is sufficiently large to avoid saturation of the device (15,16). In recent years, there has been a growing body of evidence on the feasibility of SiPM PET detectors for simultaneous PET/MR imaging (17-19), time-of-flight (TOF) information measurement (20,21), and depth-of-interaction determination (22-24).

However, the projects to implement the PET detection systems based on SiPM are still in an early stage.

In the current study, a prototype SiPM PET device with a small ring diameter was developed and characterized to show the feasibility of SiPM for in vivo PET imaging studies. The initial results of phantom and rodent studies will be presented. This is the first report on in vivo imaging with an SiPM-based PET system.

MATERIALS AND METHODS

SiPM and scintillation crystal

SSPM (SSPM_0611B4MM_PCB), an SiPM developed by Photonique SA (Geneva, Switzerland), that have been previously evaluated for its physical characteristics, including feasibility for simultaneous PET and MRI acquisition, was utilized in this study (18). The SSPM has peak sensitivity at a wavelength of 440 nm, yielding 25% single photon detection efficiency. Efficient gain and the signal rise time given in the vendor specification are 0.6×10^5 and 0.7 ns, respectively. The SSPM consists of 1,739 micro-cells with a >70% fill factor. The active area of each cell is $50 \mu\text{m} \times 50 \mu\text{m}$. The sensitive area of each SSPM_0611B4MM_PCB was 4.4 mm². In our previous study, one-to-one coupling of this device and a LYSO crystal yielded a 16% energy resolution and 1.3 ns coincidence timing resolution (18).

The scintillation crystal, which was used in this study, is the LGSO crystal ($\text{Lu}_{1.9}\text{Gd}_{0.1}\text{SiO}_4:\text{Ce}$ [LGSO]) developed by Hitachi Chemical Co., Ltd. (Ibaraki, Japan). The LGSO crystal has shown outstanding performance in our previous investigations (25,26). The scintillation decay time of this crystal is 41 ns according to the specifications. The LGSO crystal yields better energy resolution (12.7%) and higher PMT output than the LYSO and LuYAP crystals when it was coupled with a Hamamatsu H2453 PMT (25).

Characteristic evaluation of the SiPM

SiPMs use bias voltages (V) above the breakdown voltage (V_b) to achieve high gain, and the output charge of each micro-cell is proportional to $V - V_b$. In addition, V_b depends on the temperature (as the temperature raises, V_b increases). Therefore, the SiPM output signal stability depends mainly on the stability of the applied bias and temperature changes (*12,14*).

The basic experiments to test the operating stability and basic characteristics of SiPM devices have been performed. A blue light-emitting diode was used to illuminate the SiPMs with pulse duration of 25 ns and a frequency of 100 Hz through an optical filter to attenuate the light intensity. The SiPM, LED, and optical filter were placed in a light-tight box to prevent interference from environmental light. The pulse generator outputs used to produce the LED signals were also triggered to generate gate pulses with 400 ns width during which the SiPM signal was integrated using a charge-to-digital converter (QDC) module.

For each of a total of 140 SiPM devices, the stability of the output signal as a function of time was observed and the bias voltage to generate the same QDC output level (2000 QDC = 400 pC) was determined. The relationship between the bias voltage applied to the SiPM and its QDC output was also evaluated.

Detector module

The PET detector module developed in this study consists of a 4×13 array of LGSO crystals and a 2×6 SiPM array. The SiPM array was built by soldering each single SiPM onto the PCB board. The dead space between the sensitive areas of SiPMs was 2 mm between each column of the SiPM array and 1 mm between each row. Each crystal with a dimension of $1.5 \times 1.5 \times 7.0 \text{ mm}^3$ was optically-separated using a grid of a 3M-enhanced spectral reflector (ESR) polymer with a 0.065 mm thickness (25,27,28). The pitch between the crystals was 1.65 mm on average, resulting in a packing fraction of 85% for a detector module. Because the size of the front surface of the crystal did not match the sensitive area of the SiPM, and there was a dead space between the SiPMs due to the packaging, quartz with a thickness of 3 mm was inserted between the LGSO and the SiPM arrays for light sharing. The quartz thickness was optimized through the GEANT4 Monte Carlo simulation and experiments. In these optimization studies, four different quartz thicknesses were tested (2.0, 2.5, 3.0, and 3.5 mm), and the 3.0 mm thickness was selected as the optimal thickness because it yielded the most uniform distances between the crystal peaks in the flood image and light output from crystals. Optical grease (Bicron BC-630; Saint-Gobain Ceramics & Plastics) with a refractive index of 1.463 was placed at the interfaces (SiPM/quartz and quartz/crystal). Figure 1.1 shows crystal dimensions of a detector module.

Each block of LGSO/quartz/SiPM was housed using a custom-built polyoxymethylene case for stable coupling and positioning, and was

connected to a custom-made pre-amplifier board. Gap spacing between the detector modules (distance between the edges of LGSO crystal arrays) was 4.3 mm, resulting in the overall packing fraction of 71% for the detector system (Figure 1.4).

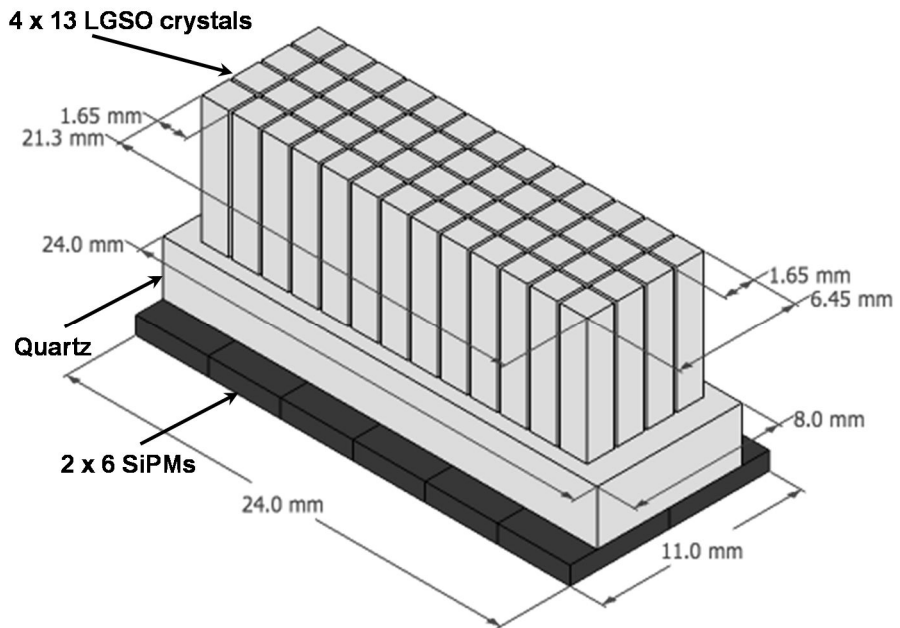


Figure 1.1 Crystal block dimension of a detector module

Readout electronics

The readout electronics developed in this study consist of a pre-amplifier board for SiPM signal amplification, a resistive charge division circuit (CDC) board for position encoding, and a voltage supply board for providing digitally-controlled bias voltage.

The pre-amplifier board consists of 12 charge-sensitive pre-amplifiers, and each of the mounted SiPMs was connected to an individual pre-amplifier, which provides a gain of ~ 25 V/V. The output current from SiPM was converted into a voltage signal, and then amplified with the second stage active amplifier modules. Each electrical component of the pre-amplifier board was optimized through the waveform analysis of the SiPM signal. On the position encoding board, the 12 pre-amplifier outputs are encoded into the 4 channels using a set of two linear resistive CDCs (Figure 1.2(a)). In each linear CDC, $100\ \Omega$ resistors interconnected 6 SiPMs in a row to obtain the X+ and X- signals, and the ratio of the column sum of each signal was used to calculate the x position in the crystal block. The y position was calculated by the ratio of the sum in each linear CDC.

The sum of four position signals was used for event triggering. Figure 1.2(b) shows an assembly of the detector block and the pre-amplifier and position-encoding boards, which were modularized to have a minimal size taking into consideration the further application to the simultaneous PET and MRI acquisition.

The high sensitivity of the SiPM output amplitude to the applied bias voltage, which will be described in detail in the Results section, has demanded

a finely adjustable and stable supply of operating voltage. Therefore, a digitally-controlled voltage supply board was developed with fine precision of 0.01-0.1 V in 64 steps through the step size variable resistor with EEPROM (DS3906; Maxim Integrated Products). In addition, a solid state temperature sensor (TCN75; Microchip Technology Inc.) was added in this module to continuously monitor the temperature change because the gain of the SiPM is also dependent on the temperature (gain and breakdown voltage variation $\sim 1.5\%/^{\circ}\text{C}$). Dedicated software, which was based on the I²C interface communication library, was developed to adjust voltage control modules and to monitor temperature information through the sensor. The software was designed to store the relationship between the optimal bias voltage to generate the same QDC output and temperature in a lookup table and to make bias voltage adjusted if the temperature changed.

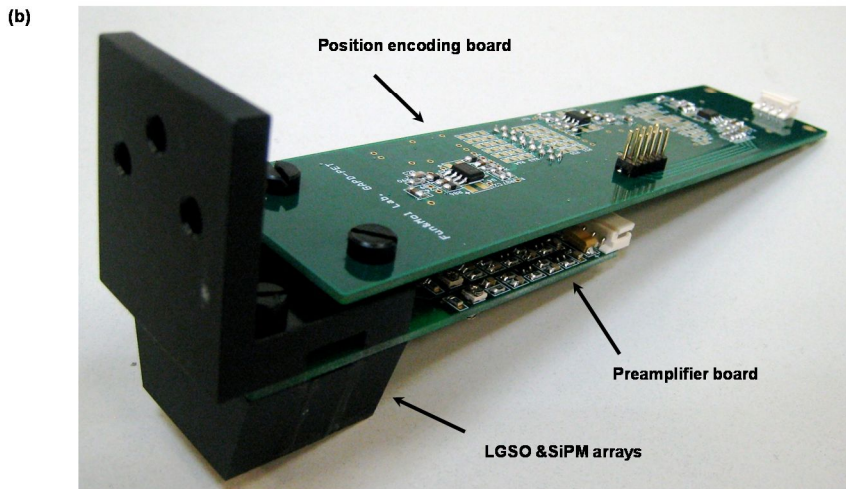
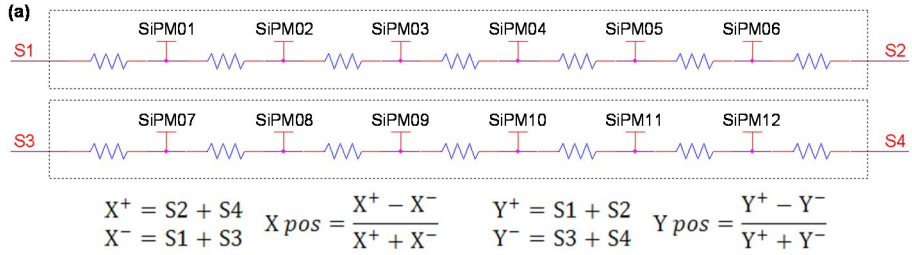


Figure 1.2 (a) Circuit diagram of position-encoding board. (c) Assembly of the LGSO/SiPM detector block, pre-amplifier, and position-encoding boards.

Prototype PET system

Figure 1.3 shows the prototype PET camera that consists of eight detector modules, and Figure 1.4 shows the schematic of the assembly of the detector modules. The detector face-to-face diameter is 6.0 cm and the distance provides the transaxial field-of-view (FOV) suitable for imaging mice. The axial FOV is 6.5 mm through 4 crystal rings (n) and 7 transaxial slices ($2n-1$). Each crystal ring consists of 104 (13×8) crystal elements. The bias voltage determined during the above “Characteristic evaluations of SiPM” section for each SiPM was applied during the data acquisition.

The encoded signals from position encoding boards were used to generate coincidence signals to measure energy and positions using nuclear instrumentation module (NIM), Versa module Europa (VME), and custom-built coincidence modules. Appropriate lengths of cables were added to ensure that signals arrived within the QDC gate. To discriminate signals and noise, constant fraction discrimination (CFD) modules (N486; CAEN) were used. To determine coincident events from the eight CFD outputs, a custom-built coincidence module implemented using a FPGA (Spartan 3; Xilinx, Inc.) was used (29). This coincidence processor module can support 28 trigger inputs, and has a minimum 2-ns coincidence time window with a 5-ns step size, and can veto the input signals after coincident detection up to 300 μ s. In addition, two 16-channel dual range multi-event QDC VME modules (V965; CAEN), which measure the integrated charges of up to 800 pC with 200 fC/bit resolution, were used.

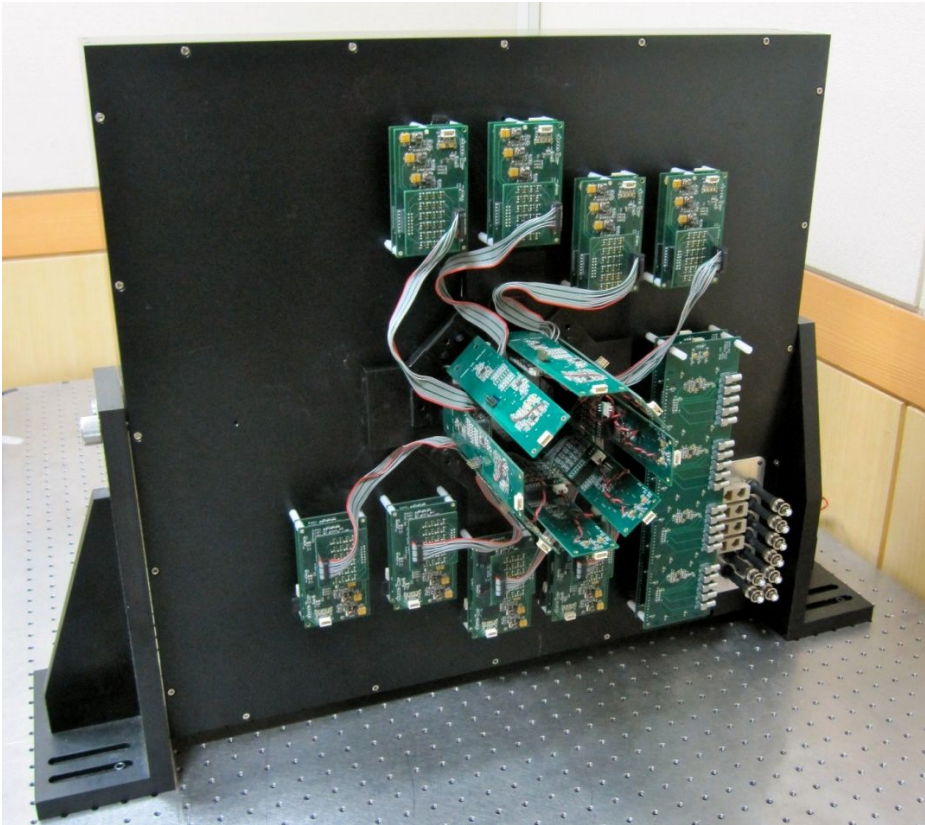


Figure 1.3 Configuration of a prototype SiPM PET camera

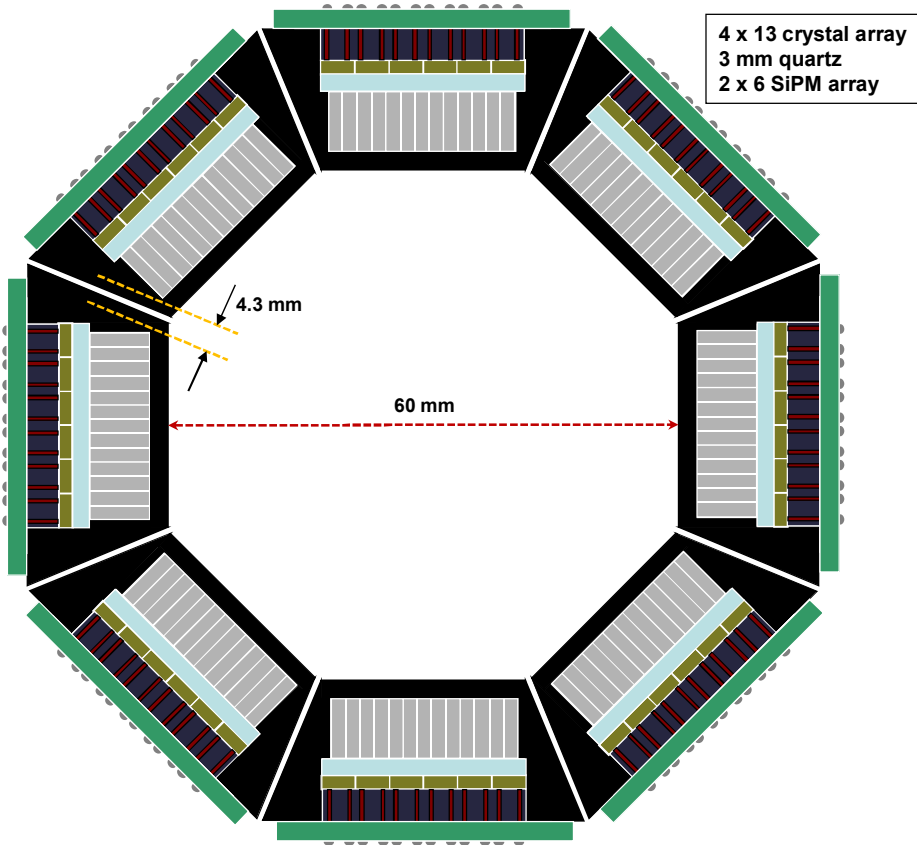


Figure 1.4 Schematic of the assembly of the detector modules

Spatial resolution and sensitivity

All PET data in this study were acquired with an energy window of 400-600 keV, except for the sensitivity measurement in which the 3 different energy window levels were applied (250-750 keV, 350-650 keV, and 400-600 keV). A coincidence window of 2 ns was applied to all the measurements.

Spatial resolution and sensitivity were measured using a ^{22}Na point source embedded in a Lucite disk (Isotope Products Laboratories).

To measure the intrinsic spatial resolution of a detector pair, the point source with a nominal diameter of 0.25 mm and an activity of 230 kBq (6.2 μCi) was placed at the center of a pair of detector modules, and moved in the transverse direction with a step size of 0.15 mm. At each location, 0.2 million coincidence counts were obtained. The coincidence counts between the individual pairs of exactly opposed crystals were plotted as a function of the source position. The count distribution of each crystal pair was fitted with a Gaussian function to determine the full widths at half maximum (FWHM) (30, 31).

The same point source was used for reconstructed image spatial resolution measurement. The point source was positioned at a 2 mm radial offset from the center of the second crystal ring and moved in a radial direction to 16 mm with a 2-mm step size. The spatial resolution was measured as the radial and tangential FWHM, which was estimated using linear interpolation method (32, 33).

Sensitivities were calculated as the ratio of the coincidence count rate and the rate at which the γ -ray pairs are emitted from the point source. A

^{22}Na point source with the activity of 2.96 MBq (63.90 μCi) and located at the scanner axis and axially moved with the step size of 0.825 mm (one-half of the axial crystal pitch) for the range of -2.475 mm to $+2.475$ mm. The point source activity was corrected for the ^{22}Na branching ratio of 0.906 (32).

Phantom study

An Ultra-Micro Hot Spot phantom (inner diameter, 2.8 cm; inside height, 2.8 cm; Data Spectrum Corp.) with hot hollow channels of different sizes (diameters: 0.75, 1.0, 1.35, 1.7, 2.0, and 2.4 mm) arranged in 6 segments was scanned. The phantom was filled with 37 MBq (1 mCi) of ^{18}F solution and scanned for 4 h. In addition, uniform cylinder PET data was acquired using the same phantom without the insert. Same scan time and activity as in the Hot Spot phantom study was employed.

Animal studies

To investigate the feasibility of the system for small animal studies, mouse and rat studies were performed using the same energy and coincidence windows as used in the phantom studies. All of the animal studies were approved by the Institutional Animal Care and Use Committee at Seoul National University. During the PET experiments, the animals were anesthetized by the continuous administration of isoflurane in oxygen.

A ^{18}F -FDG scan of a BALB/c mouse (weight = 22.2 g) bearing a murine colon carcinoma cell line (CT26) on the right shoulder was acquired. A ^{18}F -FDG (33 MBq [880 μCi]) were injected intravenously, and 50 min later a 35-min list-mode dataset was acquired. A myocardial ^{18}F -FDG scan was also acquired in another BALB/c mouse (weight = 24.5 g) for 63 min. The scan was started 46 min after intravenous injection of 16.3 MBq (440 μCi).

A bone PET image of a Sprague–Dawley rat weighing 391 g was acquired for 48 min. A PET scan was started 37 min after the intravenous injection of 48.5 MBq (1.31 mCi) ^{18}F . The head of the rat was scanned.

An ^{18}F -FDG scan of a rat brain was also acquired. A Sprague–Dawley rat weighing 352 g was positioned in the scanner with its brain centered in the FOV. ^{18}F -FDG (36.6 MBq [990 μCi]) was injected intravenously, and 70 min later 60 min of a list mode dataset was acquired.

Finally, a ^{68}Ga -RGD (angiogenesis PET imaging agent) scan of a BALB/c nude mouse (weight = 24.8 g) bearing a malignant glioma cell line (U87MG) on the left shoulder was acquired for 51 min. A PET scan was

started 15 min after the intravenous injection of 33.5 MBq (910 μ Ci) ^{68}Ga -RGD (34).

After the PET scan of each animal, the animal bed with the animal attached was manually transferred to a GE eXplore VISTA PET/CT scanner (30) to acquire a CT scan. The PET data acquired using the SiPM PET camera and CT data acquired using the VISTA scanner were co-registered and superimposed manually using FIRE software (35) that allows interactive rigid body transformation of images with 6 degrees of freedom.

In addition, the PET images acquired using the developed SiPM scanner and GE eXplore VISTA were compared. Fifty-seven min after the intravenous injection of 42.1 MBq (1.14 mCi) ^{18}F in a Sprague–Dawley rat weighing 321 g, the head of the rat was scanned using a GE eXplore VISTA PET/CT scanner for 10 min. Immediately after the scan, a 60-min PET scan was acquired using the SiPM PET. VISTA PET data were reconstructed using the 2D OSEM algorithm.

Data processing

For normalization correction, normalization scans were acquired using a cylindrical phantom with an inner diameter of 49 mm and a length of 20 mm, and filled with ^{18}F covering the entire useful FOV. Different source thicknesses were compensated for each line of response in the normalization data.

The list-mode data set was sorted into a 3D sinogram using double sampling without axial compression or sinogram mashing. The data was then rebinned into 2D data using the single slice rebinning algorithm (36).

Because of the polygonal arrangement of the detectors and the space between the detector modules, filtered backprojection reconstruction resulted in significant reconstruction artifacts. Therefore, all scanned PET data were reconstructed using maximum-likelihood expectation-maximization (MLEM) reconstruction with exact position information for each line of response (LOR) element. The system matrix for MLEM reconstruction algorithms was obtained by calculating the intersection area between the pixels and tube of the response. No resolution recovery modeling was applied. An isotropic Gaussian filter with a 0.5-mm FWHM was applied to the reconstructed images, except for the spatial resolution measurement data.

In order to avoid the over-estimation in spatial resolution measurement, uniform background data acquired using a cylindrical phantom with an inner diameter of 44.5 mm were added to the point source data before image reconstruction (37).

RESULTS

Evaluation of SiPM characteristics

Most of the tested SiPM devices (129/140) yielded stable QDC output values, as shown in Figure 1.5(a). In Figure 1.5(a) (an example of QDC output values from one of the stable SiPM) the x-axis represents the event order that is proportional to the elapsed time because light pulses with a constant pulse frequency were applied. The total duration shown in Figure 1.5(a) is 1,000 s (~15 min). The distribution of the QDC output acquired from a stable SiPM had a typical Gaussian shape. On the other hand, the remaining 11 SiPMs resulted in an inconsistent time-varying output, as shown in Figure 1.5(b), and were excluded in the further construction of detector modules.

Each of the SiPMs required different bias voltage in order to produce the same level of the QDC output. In addition, this voltage level had a relatively wide distribution, as shown in Figure 1.5(c). Figure 1.5(d) shows the relationship between the QDC output and the applied bias voltage obtained in a representative SiPM. The QDC output increased proportionally according to the applied bias voltage, being consistent with our previous findings with other types of SiPMs (16,18). The very sensitive change of the SiPM output relative to the bias voltage, as shown in Figure 1.5(d) (~ 300 QDC / 0.1 V = 60 pC / 0.1 V), led us to develop the digitally-controlled voltage supply module.

All these measurements were performed at room temperature (26°C).

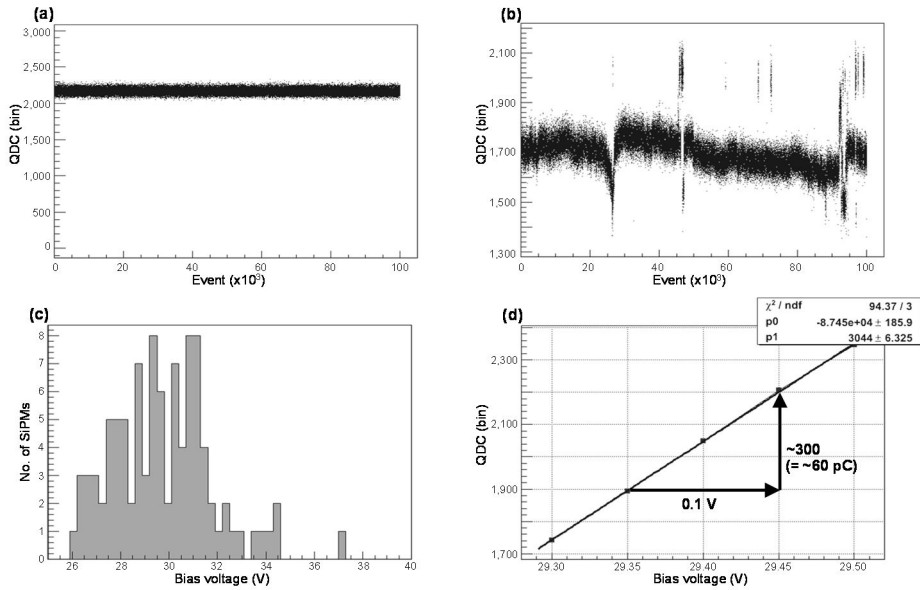


Figure 1.5 Basic characteristics of SiPM used in this study. QDC output values from one of the stable (a) and unstable (b) SiPMs as a function of time in the light-emitting diode test. (c) Wide distribution of optimal bias voltage to obtain the same level of QDC output. (d) Dependence of QDC output from SiPM on bias voltage. The straight line is a linear fit of data.

Intrinsic properties of the detector module

Figure 1.6(a) shows the flood image of a LGSO/SiPM detector module, which was obtained by irradiating the detector for 12 hours using the ^{22}Na point source (370 kBq) located 10 cm away from the detector center. All 4x13 LGSO crystals within the block are clearly distinguishable in the flood image. From the flood image, the crystal map was generated semi-automatically by searching the local peaks in the flood image and calculating the minimum distance from the peaks (26). In the flood image, corner crystals are darker than the center crystals, possibly due to the crystal interference effects, and smaller solid angle of source irradiation.

Figure 1.6(b) shows the energy spectrum of each crystal element that was calculated by accumulating the events that reach the corresponding crystal position in the crystal map. In the energy spectrum of each crystal, the photo-peak region was separated from the scattered events. The energy resolution for individual crystal was $25.8 \pm 2.6\%$ on average for 511 keV photo-peaks.

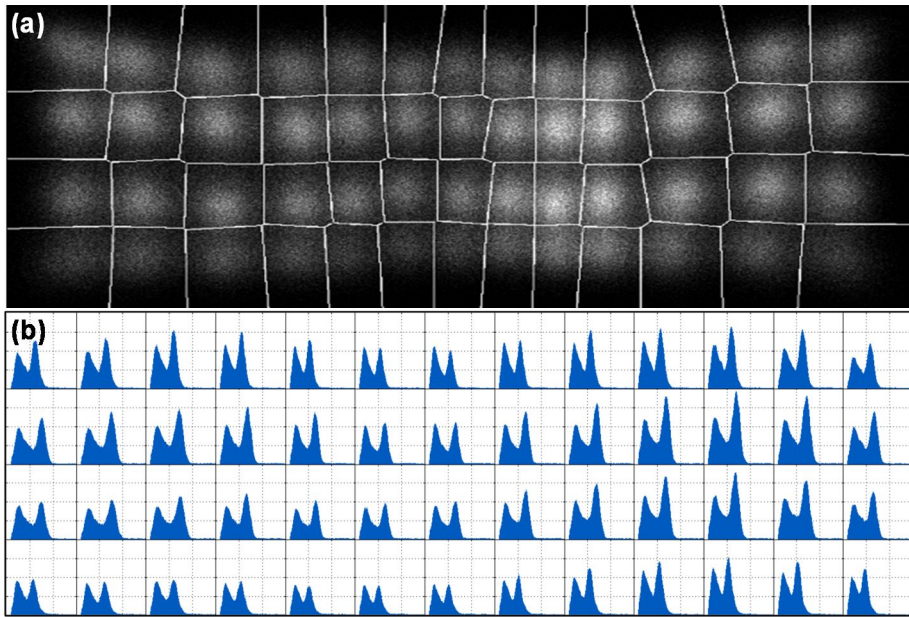


Figure 1.6 Intrinsic properties of detector module. (a) Flood map acquired using a LGSO/SiPM detector module. (b) Energy spectra of all 52 crystals in this module.

Spatial Resolution and Sensitivity

Figure 1.7(a) shows the sensitivities with various energy windows (250-750 keV, 350-650 keV, and 400-600 keV). The central plane had maximum sensitivity at each energy window (0.085%, 0.057%, and 0.040% for energy windows of 250-750 keV, 350-650 keV, and 400-600 keV, respectively).

The intrinsic spatial resolution of a typical detector pair was 1.30 mm on average (range: 1.19 - 1.49 mm). Reconstructed image spatial resolutions measured at various radial positions using a ^{22}Na point source were plotted in Figure 1.7(b). The spatial resolution was estimated after subtracting the background from the MLEM reconstruction image with 32 iteration numbers and corrected for the blurring by source diameter. The data show that 1.0 mm (2 mm off center) and 1.4 mm (16 mm off center) spatial resolutions (average of tangential and radial resolutions) can be obtained using the developed prototype SiPM PET camera.

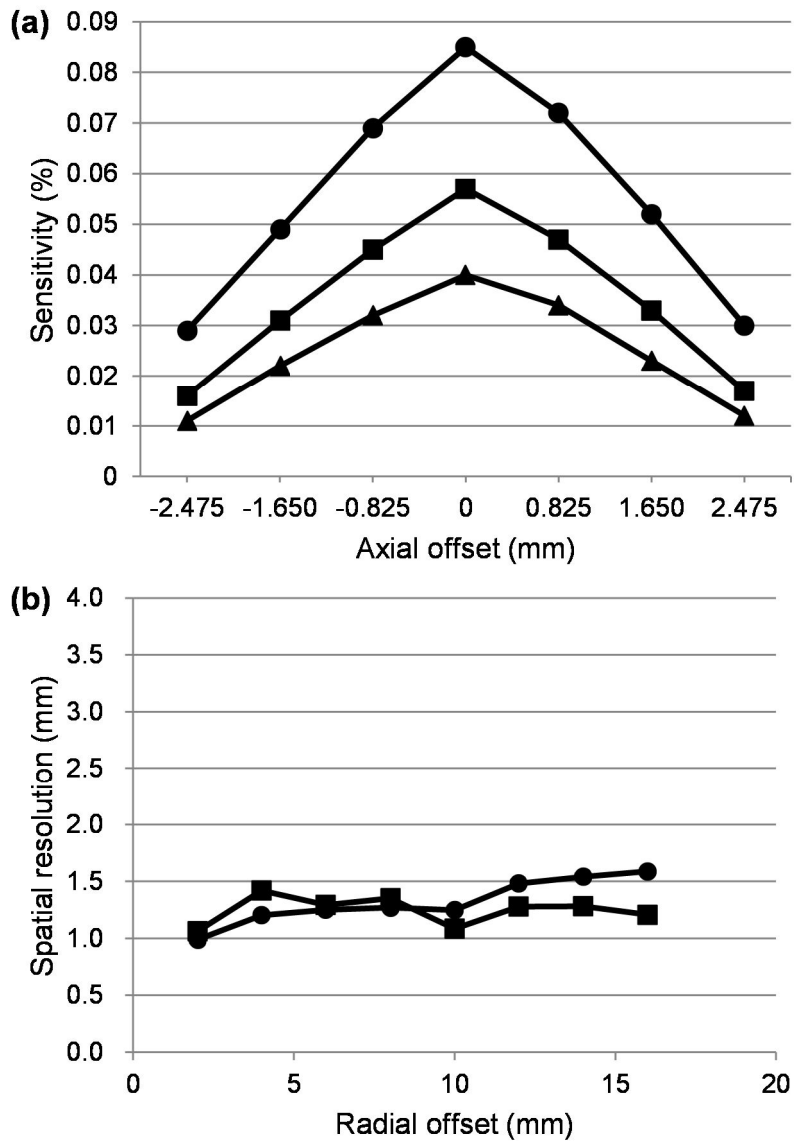


Figure 1.7 Physical performance of SiPM PET camera. (a) Sensitivity values measured at various axial offset (circle: 250-750 keV energy window; square: 350-650 keV; triangle: 400-600 keV). (b) Spatial resolution values measured at various radial offset (circle: tangential; square: radial).

Phantom and animal studies

A transaxial image (thickness = 0.825 mm) of the Ultra-Micro Hot Spot phantom with hot hollow channels is shown in Figure 1.8(a) Spots with diameters > 1.7 mm were distinguishable in this image. Although the spots with a diameter of 1.35 mm were identifiable, the separation from the background was not clear. Profile through the 1.35 mm hot spots is shown in Figure 1.8(b). A transaxial image of the uniform cylinder phantom is shown in Figure 1.9.

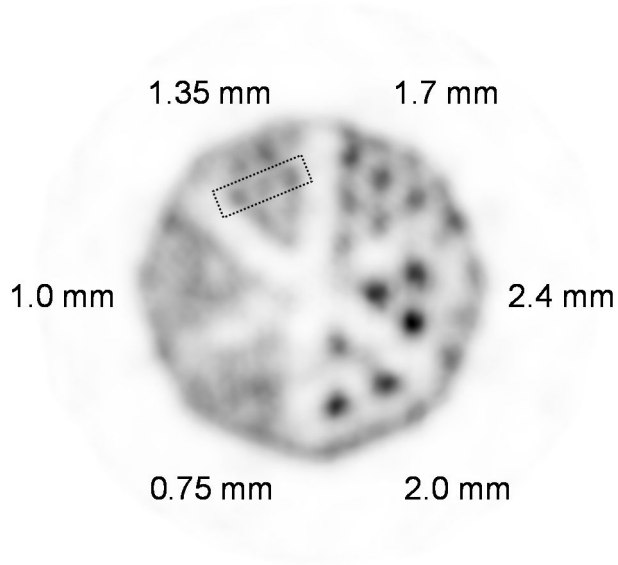
Figure 1.10(a) shows the images of a mouse bearing a colon carcinoma scanned after injection of ^{18}F -FDG (The coronal and sagittal views of fusion image are shown in Figure 1.11). Higher FDG uptake in the tumor region than the contralateral normal tissues was well-visualized in these images. The region without activity was necrotic at the center of the tumor (tumor size, ~ 1 cm). Figure 1.10(b) shows the ^{68}Ga -RGD PET image of a mouse bearing a malignant glioma cell line (an angiogenic tumor) on the left shoulder, which reveals the high uptake of ^{68}Ga -RGD.

Short axis images of the ^{18}F -FDG myocardial PET acquired without electrocardiogram gating in a mouse are shown in Figure 1.12. FDG uptake in the left ventricular myocardium is resolved well in these images, demonstrating that this prototype camera has very fine spatial resolution, which is confirmed by the profile of image shown in Figure 1.13. The truncation of images in Figure 1.12 is due to the re-orientation of images to obtain the short- and long-axis images.

Figure 1.14 shows the ^{18}F bone PET image of a rat head region. The ^{18}F activity is well-localized in the skeletal structures, as shown in the fusion image, which would be additional evidence of the fine spatial resolution of the scanner. Figure 1.14 shows the results of a rat brain ^{18}F -FDG PET study. The FDG uptake in the brain matches well with the brain areas shown on CT.

Figure 1.15 shows the ^{18}F bone PET images acquired in the same rat using the developed SiPM based scanner and a PMT-based GE eXplore VISTA scanner, indicating that equivalent PET images can be obtained using these scanners.

(a)



(b)

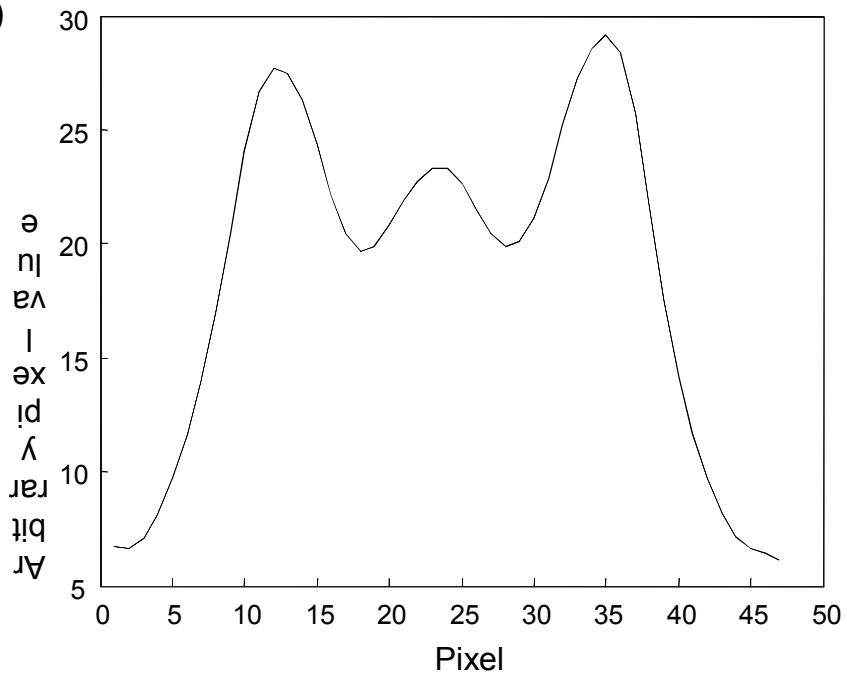


Figure 1.8 Image of Ultra-Micro Phantom with 6 hollow channels (a). The lines indicate the position of the profile shown in (b).

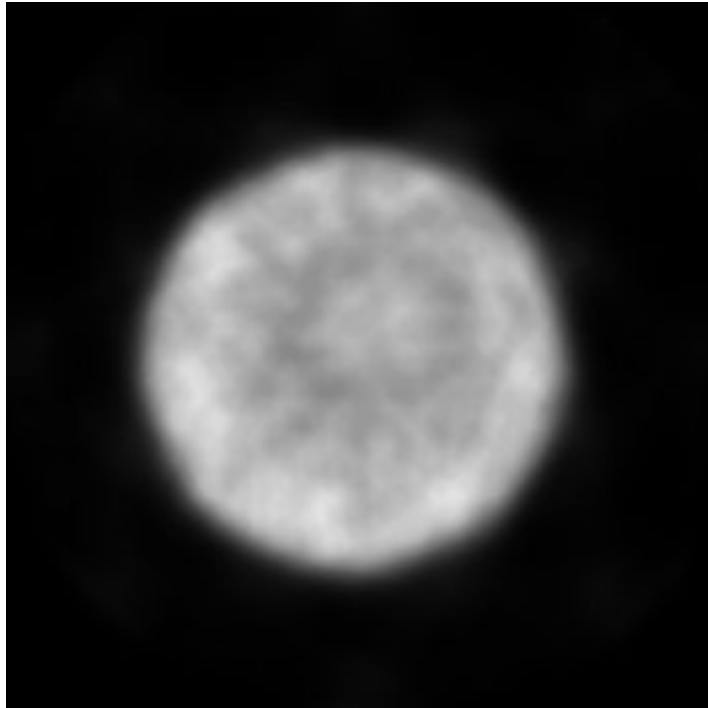


Figure 1.9 Image of a uniform cylinder phantom

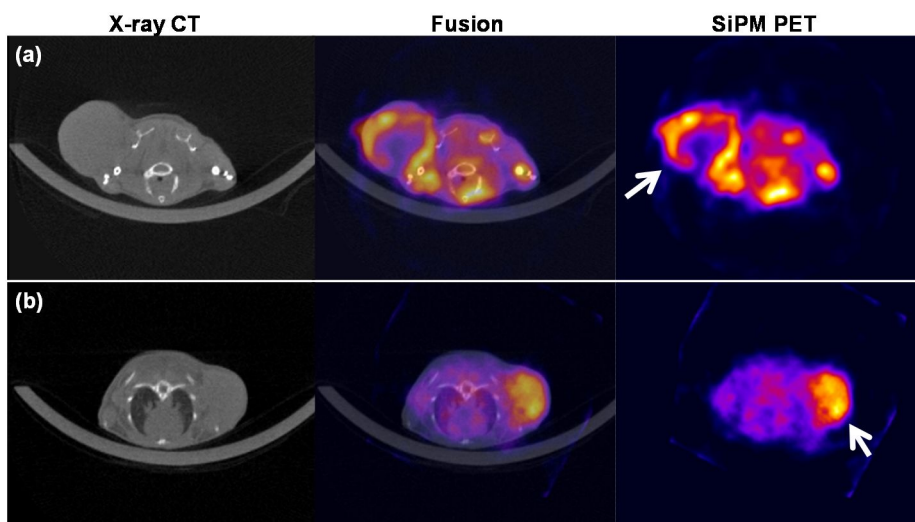


Figure 1.10 Tumor imaging in mice. (a) ^{18}F -FDG PET study in a mouse bearing a colon carcinoma. (b) ^{68}Ga -RGD PET study in a mouse bearing a malignant glioma cell line.

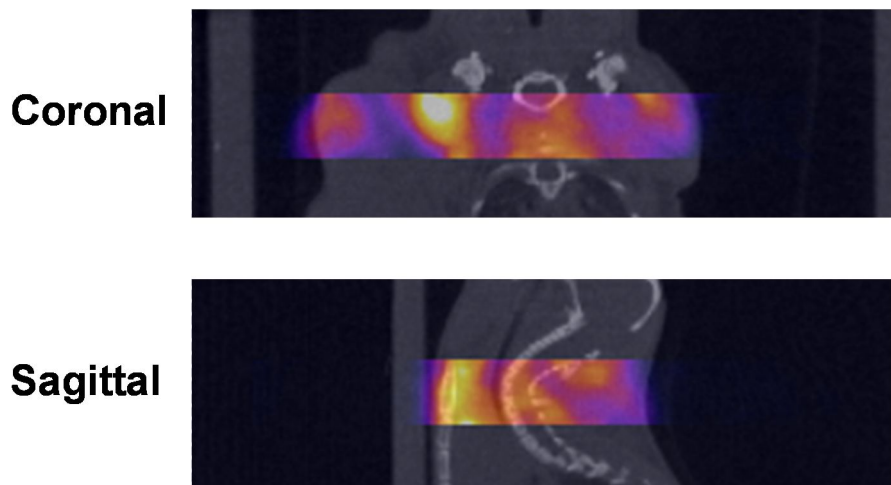


Figure 1.11 The coronal and sagittal views (fusion images) of ^{18}F -FDG PET of a mouse bearing a colon carcinoma.

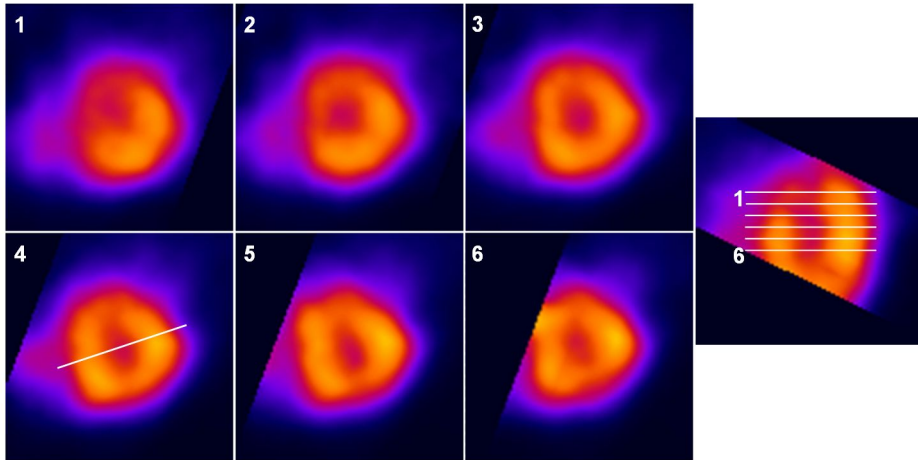


Figure 1.12 Short axis images of ^{18}F -FDG myocardial PET acquired without electrocardiogram gating in a mouse. The line on 4th plane indicates the position of the profile shown in Figure 1.13

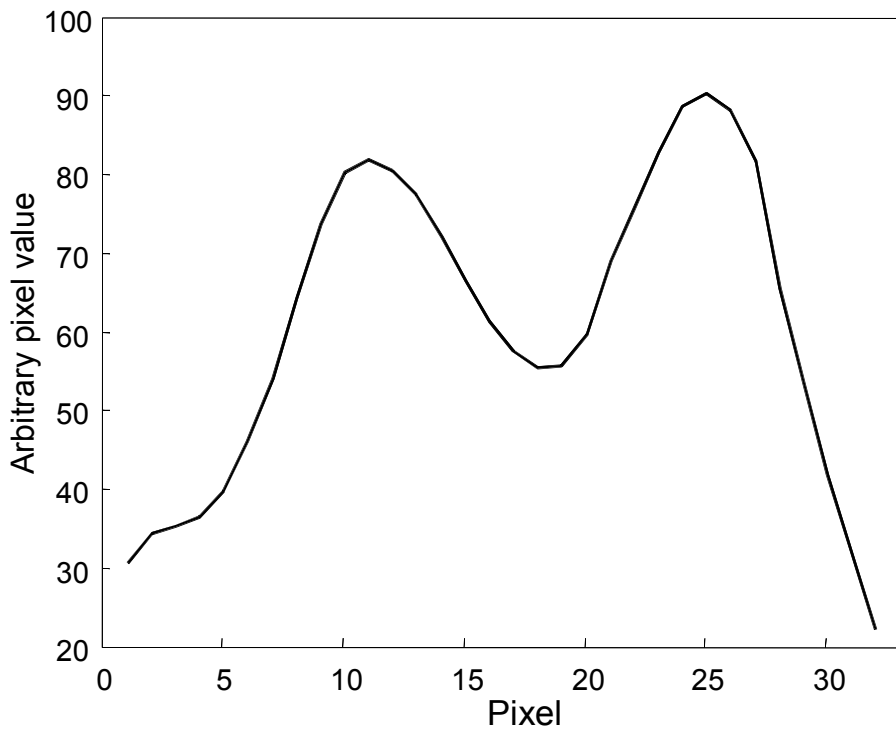


Figure 1. 13 Profile of the ^{18}F -FDG myocardial PET image in a mouse

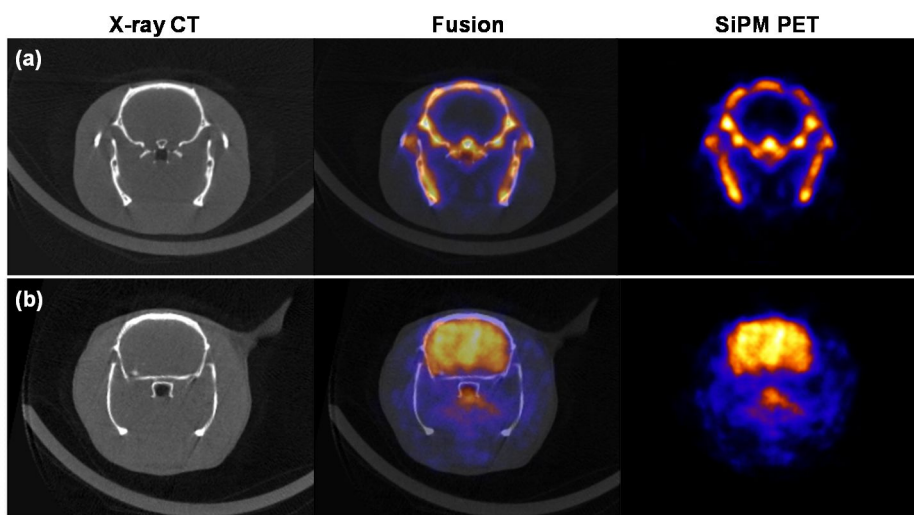


Figure 1. 14 PET images of rats. (a) ^{18}F bone PET study in a rat head region.
(b) ^{18}F -FDG PET study in a rat brain.

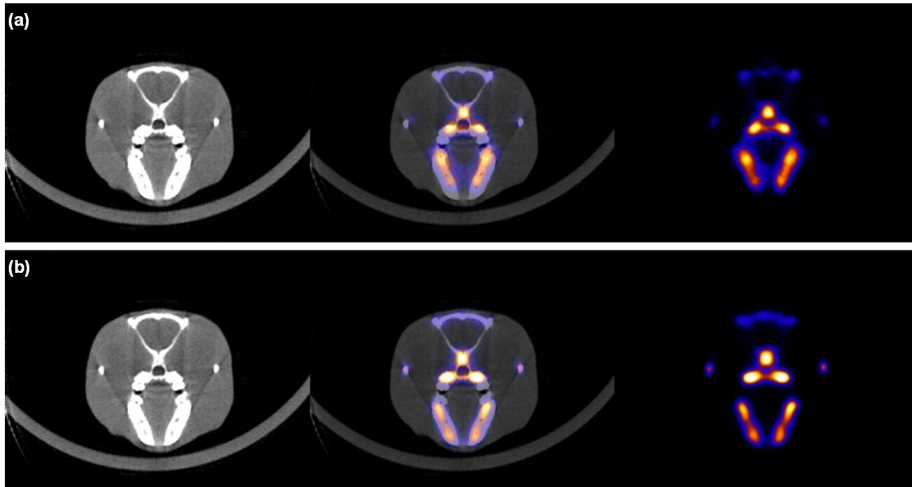


Figure 1. ^{18}F bone PET images acquired in the same rat using the developed SiPM based scanner (a) and a PMT-based GE eXplore VISTA scanner (b).

DISCUSSION

There are several reasons that SiPM is gaining attention as a promising photo-sensor in nuclear medicine imaging devices (11,14). There is no doubt that the PMT is a current workhorse in these devices. However, the PMT is not suitable for making compact-size, MR-compatible, and/or low-priced devices because of its relatively complex structures (10). Although these disadvantages of PMT can be overcome by use of the APD, it is difficult to reduce the manufacturing costs of the APD because it requires a non-standard CMOS production process (1). On the contrary, there is adequate room for reducing the manufacturing costs of the SiPM because it can be produced in a standard CMOS process, unlike the APD (10,38,39). The reduction in the SiPM price during the last several years would be evidence of this possibility. In addition to many technical advantages mentioned previously (high internal gain, fast response, small size, low power consumption, and magnetic tolerance), the potential low price of the SiPM would be the main motivation of the current active research on SiPM production and its application.

The currently used clinical whole-body PET scanner only has an axial extent of 15-20 cm, which is much shorter than the axial FOV required to be scanned in whole-body studies. This is the main reason why the current clinical PET scanners yield < 1% sensitivity and require a scan time at least 5 min for the whole-body examination. Although substantial gain in sensitivity and noise-equivalent count rates (NECRs) are possible by extending the axial

length of the PET scanner (40,41), an increase in the production cost of the PET scanner is a practical limiting factor. Accordingly, if a low-price SiPM can replace the expensive PMT and APD in the future, it will be highly useful for elongating the axial length and increasing the sensitivity and NECRs of PET scanners. Improvement in the sensitive area, which is a current limitation of SiPM, will also lead to NECR improvement through the energy and timing resolution enhancement. Moreover, the increased sensitivity and NECR will lead to a dramatic reduction in scan time and radio-pharmaceutical use.

In addition, excellent timing properties of the SiPM would warrant good PET image quality. In a previous study, our group has shown a 1-ns coincidence timing resolution using LYSO/SiPM detector pairs (18). Moreover, there is increasing evidence that SiPM is feasible for TOF measurement (11,12,20,42). A coincidence timing resolution of 240 ps can be achieved with LYSO and MPPC (SiPM provided by Hamamatsu Photonics K.K.) couplings in optimal conditions in terms of the bias voltage and temperature (21). Recently, investigators at Philips Corporate Technologies have introduced a concept of digital SiPM, which yielded a 153-ps timing resolution for LYSO crystals (43).

In the current prototype LGSO/SiPM camera, the energy resolution of the 511 keV photo-peaks was 25.8% on average for 416 crystals, which is similar to the previously reported 26% (31) and 23% (44) energy resolutions for the first commercial LSO/PMT-based animal PET scanners (microPET P4 and R4, respectively). This energy resolution is worse than the 16% that was measured using a single SiPM directly coupled with the LYSO crystal in our

previous study (18). The degradation of energy resolution may be the result of optical cross-talk that occurs mainly through the 3-mm quartz inserted between the crystal and SiPM arrays for light-sharing, and different photon detection efficiencies and amplification gains of SiPMs. However, the energy resolution degradation does not appear to be more significant for crystals near the edges of the array, as shown in Figure 1.6(b). To improve the energy resolution, the detector modules based on the one-to-one coupling of optically-isolated crystals and SiPMs need to be considered in the next stage developments.

The axial FOV of this prototype is 6.5 mm through 4 crystal rings, resulting in the very low sensitivity at the center (0.085% for an energy window of 250-750 keV). Although this size would not degrade the feasibility of SiPM PET demonstrated in this proof-of-concept study, it is not sufficiently long for routine animal scans. The rapid advances in the development of array-type SiPMs (i.e., Hamamatsu MPPC S11064 and SensL SPM 3035G16) offer the possibility of devising larger scale PET scanners with a sufficiently long axial FOV.

In this study, the developed PET system used 7.0-mm long LGSO scintillation crystals so as not to cause parallax errors for obliquely-incident γ -rays, although we knew that the detection efficiency for 511 keV γ -rays obtained with this crystal length would not be high enough. To achieve the enhancement of sensitivity by elongating crystals, depth-of-interaction (DOI) determination within crystals will be necessary to avoid the deterioration in spatial resolution uniformity (45). Several groups have shown that DOI

encoding with SiPM is a feasible technique (22-24). Implementing the DOI encoding methods suggested by our group (25,28,46) will also be possible using the SiPM arrays.

A pair of the current SiPM detector modules yielded an intrinsic spatial resolution of 1.30 mm. Fine image spatial resolution (1.0 mm at 2 mm off center) measured from the MLEM-reconstructed images of the background added point source data that has also been confirmed in small animal studies. As shown in Figure 1.15, ^{18}F bone PET images of rat skull acquired using the SiPM PET showed an equivalent level of image blurring and anatomic delineation of bone structures to the GE eXplore VISTA scanner that has a similar crystal surface area ($1.45 \times 1.45 \text{ mm}^2$) as the developed system ($1.5 \times 1.5 \text{ mm}^2$) although the SiPM PET required longer scan time due to the lower sensitivity (10 min for GE VISTA vs. 60 min for SiPM PET prototype). The non-gated mouse myocardial PET images shown in Figure 1.12 also demonstrate the fine spatial resolution of the prototype. The images are comparable to those obtained using commercial PMT-based animal PET scanners, such as the VISTA [Figure 6 in (30)] and Siemens Inveon [Figure 7 in (47)].

Although the low level of bias voltage for SiPM offers several advantages, as mentioned previously, it should be noted that the bias voltage has to be finely regulated because of this low level and the sensitivity of the gain to its stability, as shown in Figure 1.5(d). In fact, every parameter of SiPM is dependent on the bias and temperature changes, in contrast to the PMT that is against these factors (14). The digital module devised in this

study was useful in finely adjusting the gain of SiPM. In the next development, this system will be implemented on an embedded system for the real-time control of the amplifier gain or bias voltage, or the retrospective correction of the output amplitude.

CONCLUSION

All individual LGSO crystals coupled with SiPMs were clearly distinguishable in flood images, resulting in the energy resolution for individual crystals of $25.8 \pm 2.6\%$ on average for 511 keV photo-peaks. A typical detector pair yielded an intrinsic resolution of 1.30 mm. The reconstructed image spatial resolution measured with the ^{22}Na point source was 1.0 mm (2 mm off center) and 1.4 mm (16 mm off center) with the MLEM reconstruction algorithm. A myocardial ^{18}F -FDG study in mice and a skeletal ^{18}F study in rats demonstrated the fine spatial resolution of the scanner. The results obtained in this study indicate that it is possible to develop a PET camera using a promising semi-conductor photo-sensor (SiPM) which yields reasonable PET performances in phantom and animal studies.

CHAPTER 2

Time-of-Flight PET Block Detector

INTRODUCTION

Positron emission tomography (PET) is one of the most important medical imaging modalities for the visualization of the functional and molecular information of pathologic structures in the living body. The combination of PET with X-ray computed tomography (CT) enables the incorporation of more accurate anatomical information for the interpretation and analysis of PET data. Another recent advance in PET devices is the time-of-flight (TOF) information measurement capability (1,42). The TOF information on mutually annihilated photons is useful for improving the reconstructed PET image quality, reducing the radiation dose, and/or shortening the scan time (50,51,52). Gap artifact reduction in partial ring PET systems is another example of the benefits that we can derive from TOF measurements (53,54,55).

The photomultiplier tube (PMT) is the photosensor that is used in current commercially available TOF PET scanners, which yield coincidence timing resolution of ~ 500 ps at the system level. Efforts to improve the timing properties of the PMT are continuing (i.e. enhanced quantum efficiency in the photoelectric conversion process and reduced transit time spread in the electron transport). Promising results have been reported from recent studies performed with these advanced PMTs (56,57,58). However, PMTs have several well-known drawbacks, including their sensitivity to magnetic fields and their size, which is much larger than the individual pixelated scintillation crystals used in current PET systems.

Meanwhile, the silicon photomultiplier (SiPM) is a promising semiconductor photosensor for future use in both TOF PET/CT and PET/magnetic resonance imaging (MRI) scanners because the SiPM is insensitive to magnetic fields and has internal gain and timing properties that are compatible with the PMT (12,59). It also has a compact size that enables direct one-to-one coupling between the scintillation crystal and the photosensor, yielding better timing and energy resolutions than the light sharing methods that are currently used in PMT PET systems. Recently, many encouraging results showing the feasibility of using the SiPM for PET applications have been reported at both detector and system levels (60,61,62, 63,64). The excellent timing resolution of SiPM-based PET detectors reported recently in the literature also warrants the realization of MR-compatible TOF PET scanners with better timing resolution than the current level (21,49,65).

Although one-to-one coupling between the scintillation crystal and the SiPM has the advantages mentioned above, this method requires a huge volume of readout and processing electronics if no electrical signal multiplexing or encoding scheme is properly applied. Therefore, in this study, we propose an electric signal encoding scheme compact data readout scheme using FPGA without ADC for SiPM array based TOF PET detector blocks; with this scheme, we can reduce the complexity and volume of the signal readout and processing electronics. I evaluated the effects of the SiPM array size on the timing and energy resolutions of the proposed detector block, because the combination of the multiple SiPM channels results in a higher dark count rate that has potential adverse effects on the physical performance.

I also developed multi-channel digital time-to-digital converter (TDC) implemented on FPGA evaluation board and measured the basic performance.

MATERIALS AND METHODS

Concept of proposed TOF SiPM PET block detector

Proposed TOF SiPM PET block detectors are comprised of several $M \times N$ SiPM array blocks and an FPGA board (Figure 2.1).

In an $M \times N$ SiPM array, the output signal of each SiPM channel that is directly coupled to the pixelated scintillation crystal is divided into two signal lines. These output lines are tied together in row and column lines (66). These row and column signals are used to measure the energy and timing information (or vice versa) of each incident γ -ray event, respectively. The 2D position of the γ -ray interaction is determined by a combination of the row and column signals. By applying this method, the number of output channels is reduced from $M \times N$ to $M + N$. The easy extendibility of this method with its flexible array size provides another advantage.

Each of the row and column signal lines would then be connected to an amplifier stage. Amplifier stages with different characteristics that are suitable for either energy or timing measurement would be preferred (65). Simple inverting or non-inverting amplifiers and complex multi-stage amplifiers, such as differentiators and high-order shaping filters, can all be used in the amplifier stages. Each output signal of row and column amplifier stages would then be connected to a comparator. The output signals are converted into digital signals in these comparators with certain threshold voltages. The converted digital signals are transferred to an FPGA board through the high-speed cables.

Multi-channel digital time-to-digital converters (TDCs) are implemented on the FPGA to measure precise time from transferred signals. Time and energy of incident γ -ray are measured from converted column and row signals using digital TDC on FPGA, respectively. To measure the energy using only time measurement module without ADC or QDC, time-over-threshold (TOT) method are used. TOT method is to measure the time duration of the pulse over the certain threshold voltage. This time duration is approximately proportional to the energy value in certain range of measured energy. Because the same modules are used, we can simultaneously achieve the results of energy and time information for one incident γ -ray event without waiting on each other. The FPGA board also has signal process unit for decide valid event filtering and communication unit for data transfer to other devices.

However, it must be noted that too large an array size and too high an encoding ratio can lead to degradation of the timing and energy resolutions and the count rate performance because of the increased dark count rate, resistance-capacitance (RC) value, signal pass length difference, and dead time loss. Therefore, careful evaluation of the performances of the detector blocks with different array sizes is necessary to balance the signal encoding ratio and the detector performance.

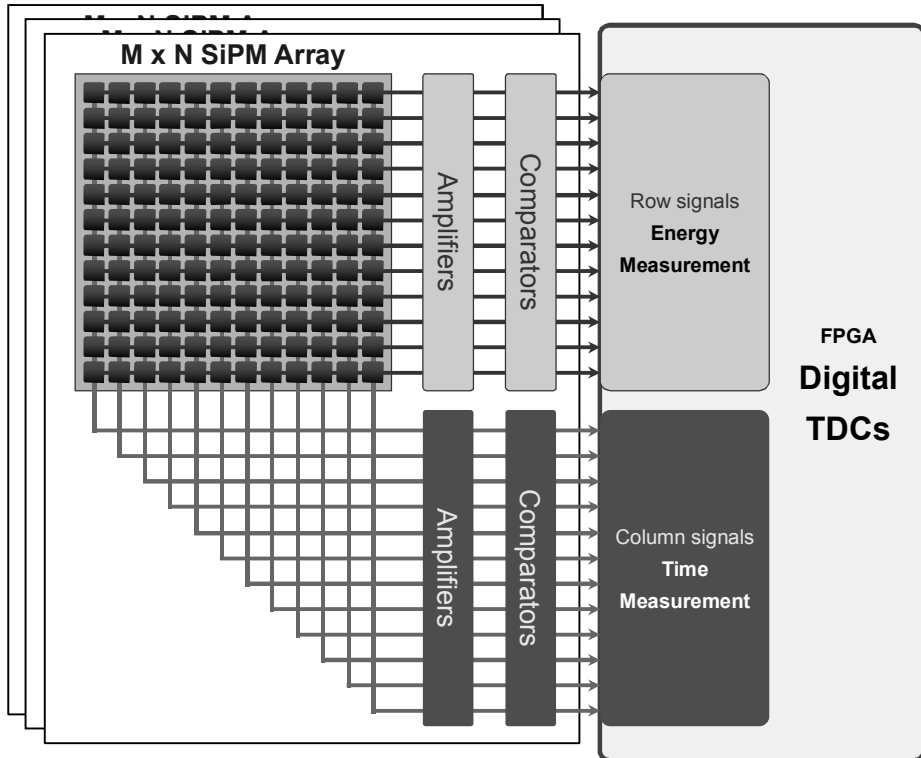


Figure 2.1 Conceptual diagram of the proposed signal encoding method. Output signals from the SiPM channels are tied together in row and column lines. The row and column signals are used to measure the energy and timing information of each incident γ -ray event, respectively.

Front-end electronics and crystal block for signals encoding method concept verification

Dedicated front-end electronics for testing of the proposed signal encoding method were developed on a printed circuit board (Figure 2.2(a)). For concept verification, 4×4 channel SiPM devices (MPPC S11064-050P, Hamamatsu Photonics K.K., Japan) were used to assemble an up to 12×12 SiPM array. Each SiPM channel has an active area of $3 \times 3 \text{ mm}^2$, consisting of 3600 pixels with a size of $50 \times 50 \text{ }\mu\text{m}^2$ (63,64,67). Each of the row and column signals was amplified using a high speed and high bandwidth amplifier with a simple inverting scheme. The gain of the column amplifiers ($\times 10$) was set to be higher than that of the row amplifiers ($\times 4$) for improved timing performance (21,65). The output signal of each amplifier was connected with a LEMO cable connector.

While all the SiPM cathodes were connected to a common high voltage supply, each SiPM anode was connected to each of the output channels of the digital-to-analog (DAC) converter (octal, 16 bit, buffered voltage output type). The magnitude of the DAC output was controlled by using dedicated software via an I²C (inter-integrated circuit) interface to provide different bias voltage levels that are optimized for each SiPM.

Each SiPM channel was directly coupled to a $3 \times 3 \times 20 \text{ mm}^3$ LGSO crystal ($\text{Lu}_{1.9}\text{Gd}_{0.1}\text{SiO}_4\text{:Ce}$; Hitachi Chemical Co., Ltd, Japan), which was wrapped with a 3M-enhanced spectral reflector (ESR) polymer with a thickness of 0.065 mm. Optical grease (Saint-Gobain BC-630, refractive index of 1.465) was used to optically couple the crystal to the SiPM. To match

the pitch of the crystal array with that of the SiPM array (the vertical and horizontal pitches were 4.50 mm and 4.05 mm, respectively), the crystal array was assembled using an acrylonitrile butadiene styrene (ABS) frame constructed with a 3D printer (Mojo, Stratasys, USA). Figure 2.2(b) and (c) show the 12×12 LGSO crystals held by the ABS frame and its dimension.

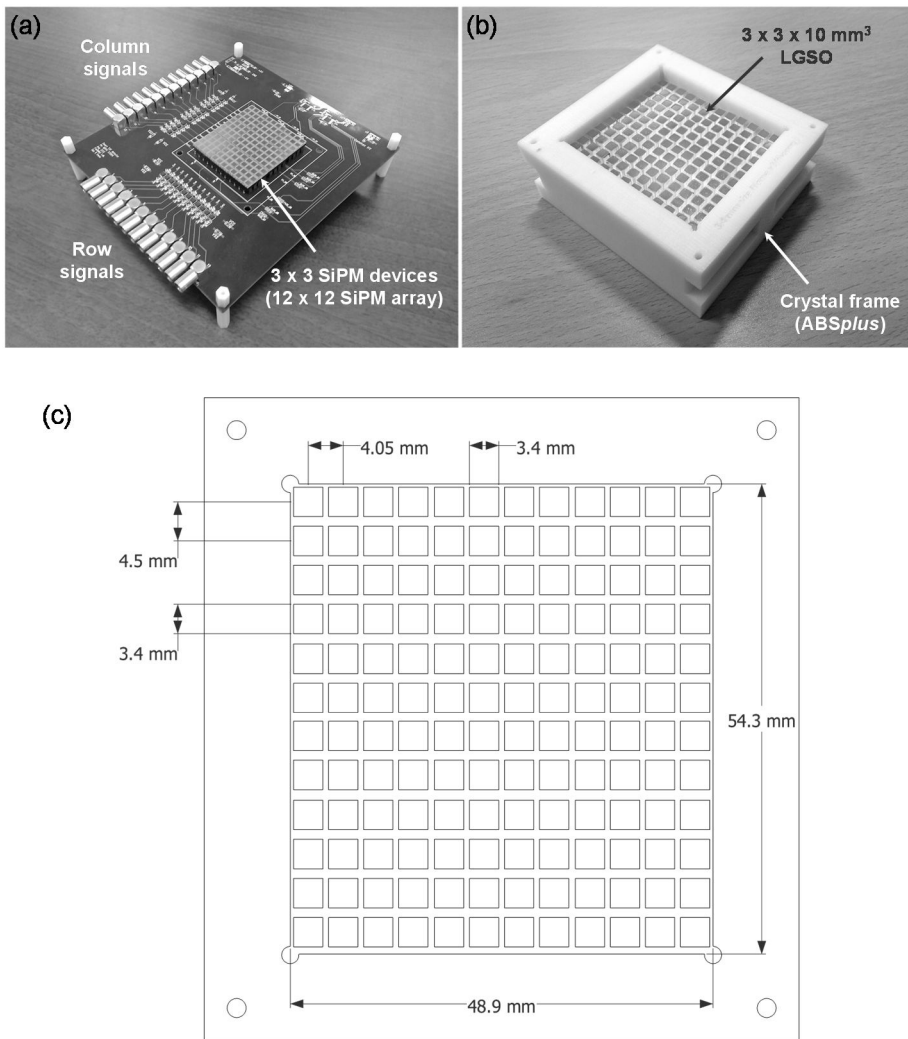


Figure 2.2 Front-end electronics circuit board implemented for testing of the proposed signal encoding method (a), the LGSO crystal array (b), and dimension of a crystal frame (c).

Measurements for verification of signal encoding method

Figure 2.3 shows the test setup for performance measurement of the developed detector block with its front-end electronics using a ^{22}Na point source (diameter < 0.3 mm). A reference detector was used to detect the coincidental γ -ray events only. The reference detector consisted of an R9800 fast PMT (Hamamatsu Photonics K.K.) and a $4 \times 4 \times 10$ mm³ LYSO crystal, which was wrapped with a 3M-ESR polymer (58). The reference detector has a single time resolution of ~ 200 ps, which was measured with a bias voltage of 1300 V and a threshold level of $\sim 3\%$ in a leading edge discriminator (LED).

Because the properties of the SiPM output depend on the operating temperature (12,59), the developed and reference detectors were placed in a temperature-controlled box with a constant temperature of 20°C. All output signals from the two detectors emerged from the box through a small hole (diameter; ~ 5 cm). To discriminate between the signals and the noise from each detector, LED NIMs (nuclear instrument modules, N840, CAEN, Italy) were used. The LED output pulses were used to determine coincidence events and to obtain the timing information of the incident γ -rays. The coincidence events were determined by using an AND NIM module (N455, CAEN), and the output pulses of the AND module generated gate pulses using a gate module (N93B, CAEN). These gate pulses were then used to integrate the input pulses from each of the detectors for energy measurement in a charge-to-digital converter (QDC) VME module (V965, CAEN). The gate pulses were also used as common-stop pulses in a time-to-digital converter (TDC)

VME module (V775N, CAEN) to measure the time information of the coincidence signals. The TDC module measures time differences of up to 140 ns with 35 ps/bit resolution. The output pulses from the LED were used as start signals for the TDC. Appropriate cable lengths were added to the QDC inputs to ensure that the SiPM signals arrive within the gate pulses.

The breakdown voltages of all the SiPM channels were estimated, because most of the properties of the SiPM output are related to the breakdown voltage (12,21). The timing resolution of the SiPM detector was then measured under different bias voltages and trigger threshold levels to find the optimal bias voltage for each SiPM. The timing and energy performance of the developed detector blocks were also measured for various SiPM array sizes (4×4 , 8×8 , and 12×12).

Concept evaluation of signal encoding methods and digital TDCs

Another front-end electronics circuit board was developed to connect SiPM detector module with multi-channel digital TDC implemented on FPGA. The front-end board consisted of one 16-channel SiPM (MPPC S11064-050P), high-speed operational amplifiers, ultra-fast comparators, and a digital to analog converter (DAC). Signal on each of row and column lines was processed with two amplifiers and a comparator. Differential output signals from comparators were then transferred to FPGA board via 1-m high bandwidth twisted data cable (CAT7). All signal lines from front-end board were carefully routed to reduce time mismatch.

The DAC was used to provide threshold voltage for each comparator with very high precision. This was the low power, octal, 16 bit, and buffered voltage-output DAC and controlled with I²C serial interface. Comparators are used to convert signal from analog to digital at certain threshold voltage, which was provided from the DAC. Time and energy information are obtained from these converted signals in FPGA. High performance comparators with the low deterministic (10 ps) and random jitters (200 fs) were used.

The crystal array consists of 4×4 polished LGSO scintillator, which was the same crystal with previous experiments. Each crystal was also wrapped with 3M ESR polymer. Optical grease was used to optically couple the crystal array to SiPM (Figure 2.4(a)). The front-end circuit board and crystal array is shown in Figure 2.4(b).

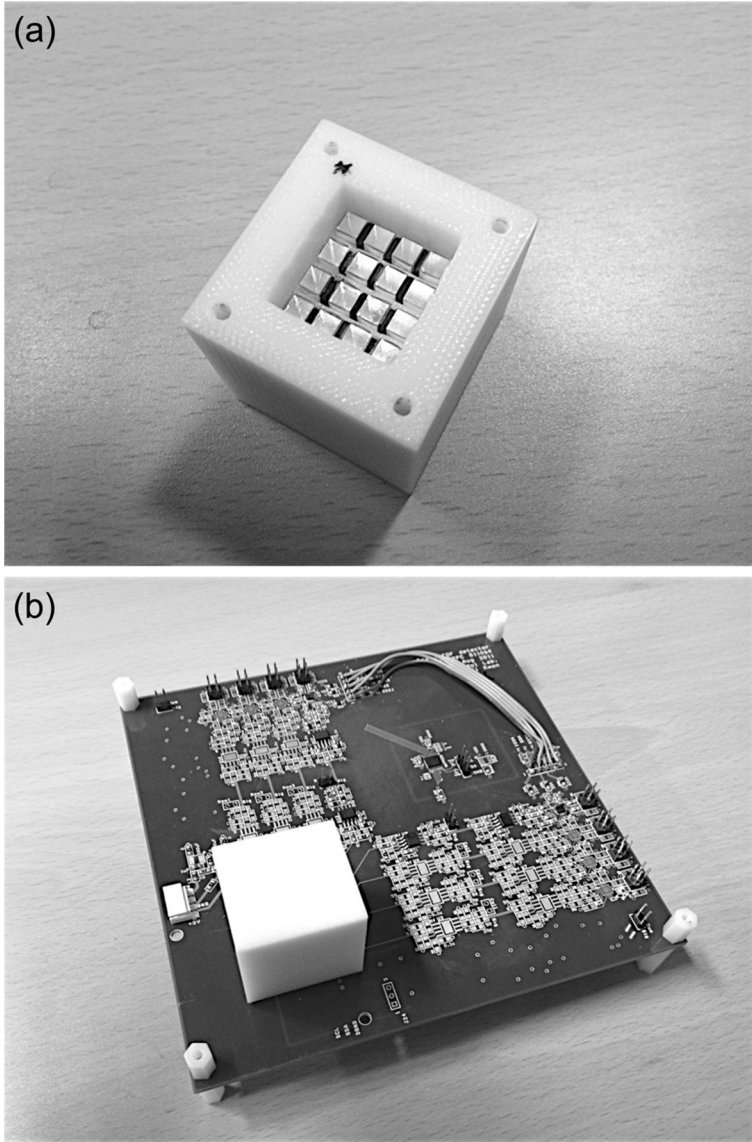


Figure 2.4 4×4 LGSO crystal ($3 \times 3 \times 20 \text{ mm}^3$) array and crystal holding frame (a) and proposed block detector – front-end board with crystal frame (b).

Multi-channel digital TDC implemented on FPGA

Multi-channel digital time-to-digital converter (TDC) using FPGA was developed on VIRTEX-6 (Xilinx, USA) evaluation board (ML605, Xilinx). Multi-channel digital TDC consisted of a global coarse counter and a number of fine counters. A set of time measurement output was obtained with coarse time from global coarse counter value and precise time from fine counter value of each digital TDC channel. The global coarse counter value was measured from stable clock generator in VIRTEX-6. The fine counter was based on the tapped delay line method. The developed fine counter can measure rising and falling time values. This can measure not only time differences among channels (for TOF) but also signal widths (for TOT) in one channel at the same time with high time precision and cost-effective component usages.

Dedicated signal receiver-board was also made to collect row and column signals from front-end circuit boards. The receiver-board was connected to FPGA board via FMC connector, which provides high timing performance. To consider the reliability of timing information, temperature data were collected from the internal FPGA sensor.

Characteristics of proposed structure

To investigate the feasibility of the TOT method for energy measurement in PET system, various radiation sources were measured using developed front-end board and digital TDC on FPGA. Only one channel of SiPM, which was coupled with a $3 \times 3 \times 20 \text{ mm}^3$ LGSO crystal, was used to measure TOT value. The threshold voltage for a comparator was fixed with certain voltage. The dependence of TOT value on γ -ray energy was obtained with ^{131}I (362 keV), ^{22}Na (511 keV), and ^{137}Cs (662 keV).

To evaluate the intrinsic timing performance of proposed structure, timing resolution was measured using developed multi-channel digital TDC and two front-end circuit boards without SiPMs. The square pulse was provided to each front-end circuit board through CAEN N401 NIM FAN IN/OUT modules. The square pulse was generated from Tektronix AFG320. Developed multi-channel digital TDC measured a timing resolution between two front-end boards. To realize the dependency of transfer cable length, two different length CAT7 cables (1-m and 3-m) were tested.

Performance evaluation of the proposed structure

Figure 2.5 shows the test setup to obtain coincident γ -ray events using one multi-channel digital TDC on FPGA, two front-end circuit boards, and ^{22}Na point source. The first front-end board was only connected to the board with one channel of a SiPM, which was coupled with a $3 \times 3 \times 20 \text{ mm}^3$ LGSO crystal, and worked as a reference single detector of SiPM. The second one was fully connected with all SiPM channels, but only one channel was coupled with a $3 \times 3 \times 20 \text{ mm}^3$ LGSO crystal. This configuration can evaluate the interferences with intrinsic noise from other SiPM channels. Energy and timing resolution were measured to evaluate the proposed structure in temperature controlled environment (20 °C).

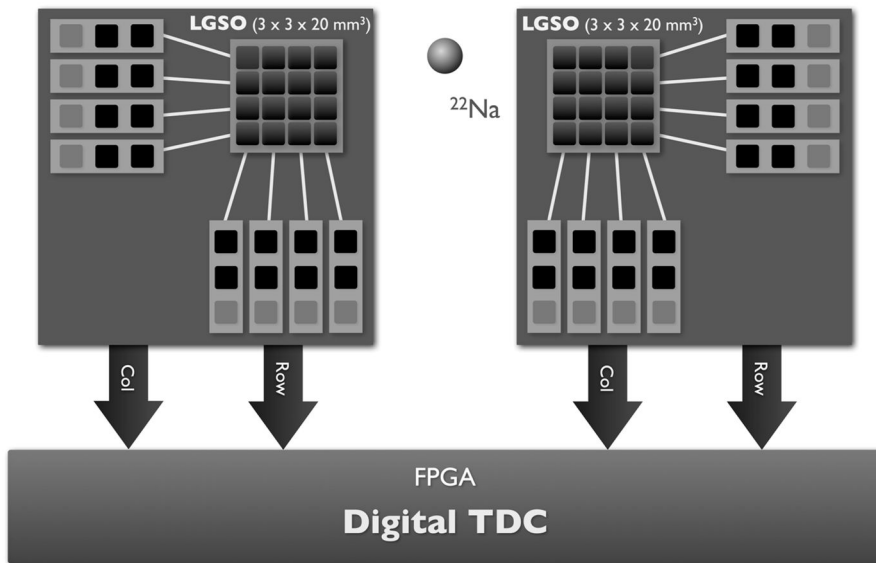


Figure 2.5 Test setup to measure coincidence γ -ray events.

RESULTS

Determination of optimal bias voltages

To find the breakdown voltages, energy spectra were obtained under various bias voltages with 0.2 V steps for all 144 SiPMs. Figure 2.6 shows the energy spectra for a typical SiPM device, which consists of 4×4 SiPM channels. The photo-peak position was selected in each spectrum and was then plotted against bias voltage for all SiPM channels (Figure 2.7). All of the plots fitted well with a second order polynomial curve ($R^2 > 0.99$). The breakdown voltage was defined as the zero-crossing point of the fitted curve in each plot of photo-peak position versus bias voltage.

Figure 2.8 shows the breakdown voltage distribution for a 12×12 SiPM array. The breakdown voltage was uniform across the SiPM channels in every SiPM device. Therefore, the average breakdown voltage for each SiPM device (as shown in table 1) was used in further experiments to simplify the bias voltage supply scheme.

In one SiPM channel of each device, the coincidence time resolutions were measured at various overvoltage levels with 0.2 V steps under different LED threshold levels (i.e. 1.5%, 3.0%, 4.5%, and 6.0% of the 511 keV energy peak). The overvoltage is the difference between the applied bias and breakdown voltages. Figure 2.9 shows the coincidence time resolutions of one SiPM channel from each device as a function of the overvoltage under different LED thresholds. The same overvoltage range, from 1.8 to 2.4 V, yielded stable and good coincidence time resolution values

for all LED threshold levels. Therefore, a 2.2 V overvoltage was supplied to each SiPM device (see table 1) and an LED threshold level of $\sim 3\%$ was applied to each of the timing measurement signal lines.

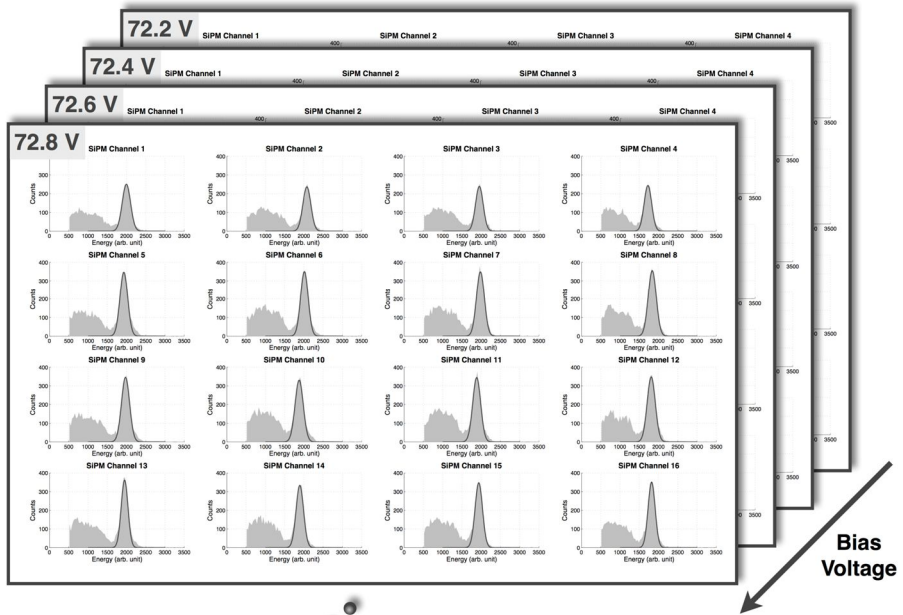


Figure 2.6 Energy spectra for a single SiPM device, which consists of 4×4 SiPM channels.

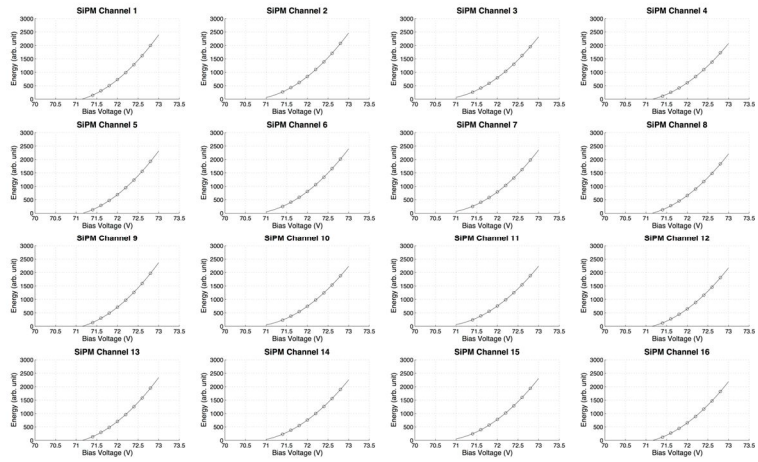


Figure 2.7 Photo-peak positions of the energy spectra as functions of bias voltage for a typical SiPM device. The plots fitted well with a second-order polynomial curve. The breakdown voltage was defined as the zero-crossing point of a fitted curve.

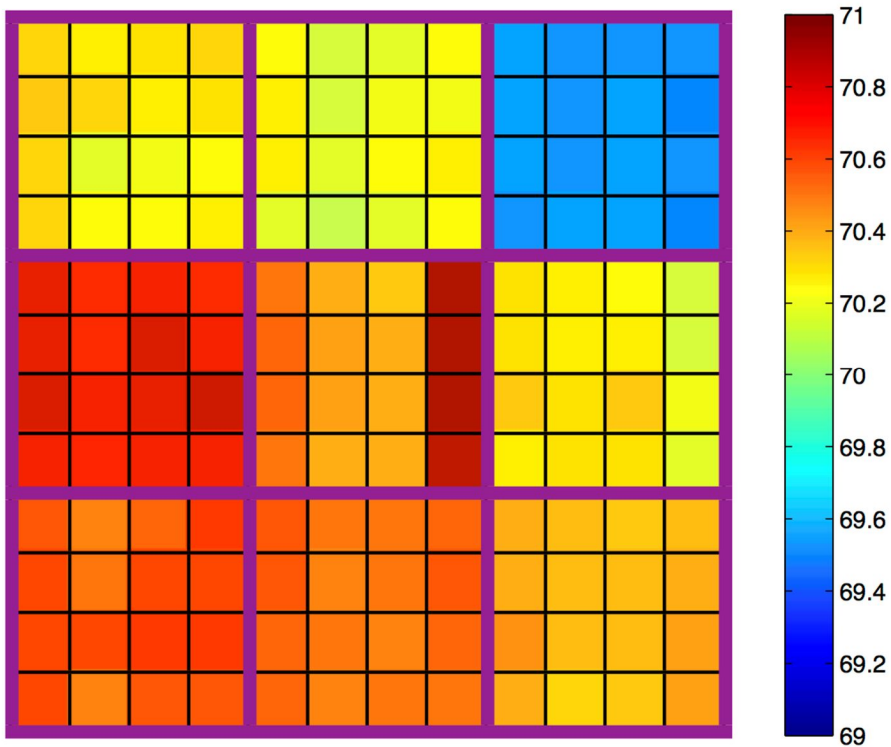


Figure 2.8 Breakdown voltage distribution of each channel in all 12×12 SiPM arrays. The SiPM channels in each of the SiPM devices (packaged by a solid line) showed uniform breakdown voltage distributions (unit of color bar: [V]).

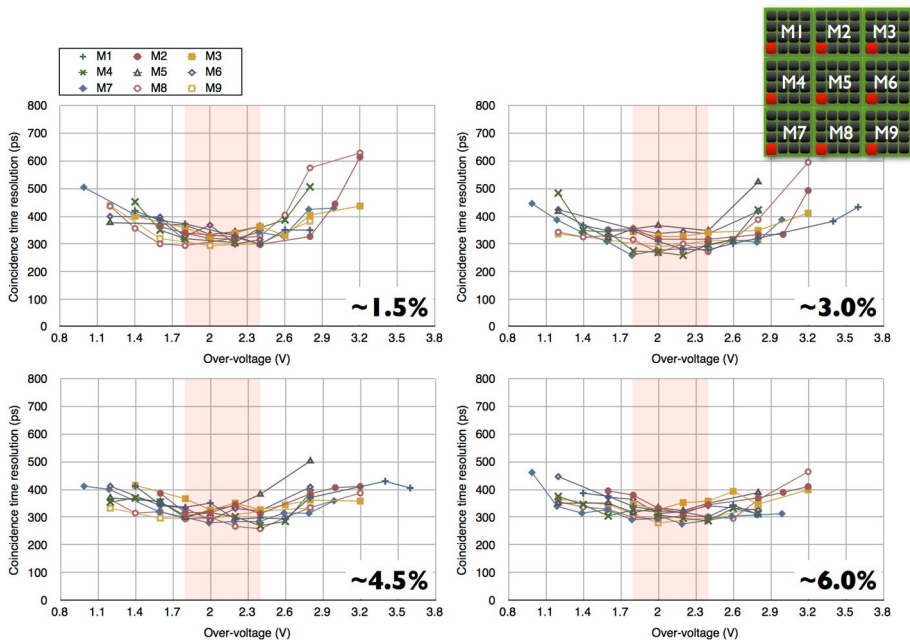


Figure 2.9 Coincidence time resolutions for one SiPM channel from each device as a function of overvoltage under different LED thresholds.

Table 1 Average breakdown voltage and +2.2 V overvoltage for each SiPM device, which was supplied to the circuit board developed for the performance measurements.

SiPM device number	Break-down voltage (V)	+2.2 V over-voltage (V)
1	70.28	72.48
2	70.20	72.40
3	69.50	71.70
4	70.77	72.97
5	70.58	72.78
6	70.26	72.46
7	70.61	72.81
8	70.56	72.76
9	70.40	72.60

Coincidence time resolution and energy resolution of various SiPM array sizes

To evaluate the proposed method, the coincidence time resolution values were measured using various SiPM array sizes (4×4 , 8×8 , and 12×12). These SiPM arrays consist of 1, 4 (2×2), and 9 (3×3) SiPM devices. While all nine SiPM devices were assembled together on the test circuit board, SiPM devices that were not used for the evaluation of smaller array sizes were turned off during these measurements.

Figure 2.10(a) shows the coincidence time resolution distribution for all of the 4×4 SiPM arrays. The average coincidence time resolution of the 4×4 SiPM arrays was 311 ps. Four SiPM devices (index numbers: 4, 5, 7, 8 [dashed box in Figure 2.10(a)]) were used to measure the coincidence time resolutions of the 8×8 SiPM array. Figure 2.10(b) shows the coincidence time resolution distribution of the 8×8 SiPM array. The average coincidence time resolution of the 8×8 SiPM array was 320 ± 31 ps. The 12×12 SiPM array distribution was shown in Figure 2.10(c) and its average coincidence time resolution was 335 ± 28 ps. Table 2 shows the single time resolution of SiPM detectors which were calculated by the convolution-subtraction of the single time resolution of reference detector (200 ps), and the expected coincidence time resolutions of two SiPM detectors with same array size (58).

The energy resolutions of the various SiPM array sizes were also measured. Figure 2.11 shows the energy resolution distributions of the 4×4 , 8×8 , and 12×12 SiPM arrays; the average energy resolutions of these SiPM arrays were 11.8%, 12.5%, and 12.8%, respectively.

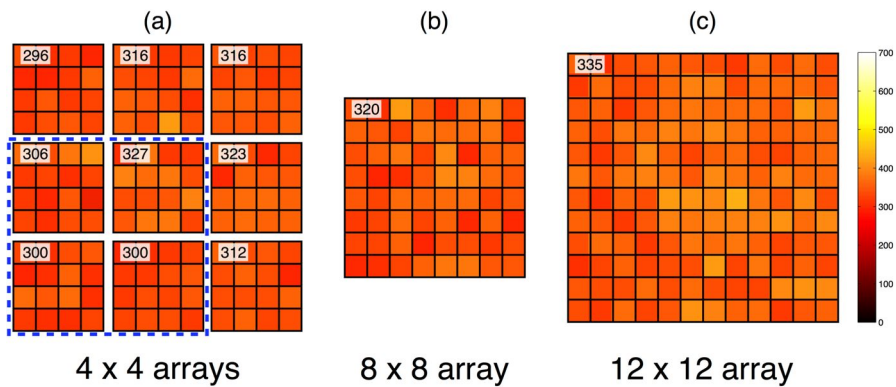


Figure 2.10 Distribution of the coincidence time resolutions of nine 4×4 SiPM arrays (a), an 8×8 SiPM array (b), and a 12×12 SiPM array (c); the average coincidence time resolutions were 311 ps, 320 ps, and 335 ps, respectively. The blue dashed box indicates the SiPM devices used in the 8×8 SiPM array.

Table 2 Measured average coincidence time resolution between SiPM detectors and reference PMT detector, and calculated single and coincidence time resolutions of SiPM detectors. Single time resolution of the reference PMT detector was 200 ps.

SiPM array size	Coincidence time resolution (ps) SiPM - PMT	Single time resolution (ps) SiPM	Coincidence time resolution (ps) SiPM - SiPM
4 × 4	316	245	346
8 × 8	320	250	353
12 × 12	335	269	380

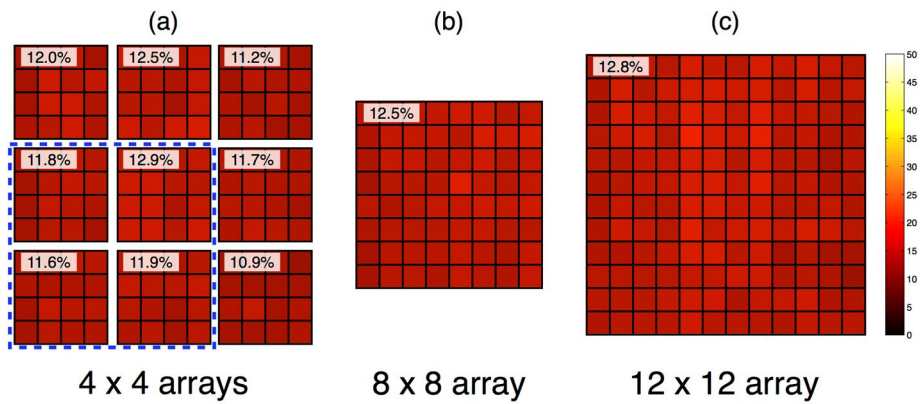


Figure 2.11 Distribution of the energy resolutions of nine 4×4 SiPM arrays (a), an 8×8 SiPM array (b), and a 12×12 SiPM array (c); the average coincidence time resolutions were 11.8%, 12.5%, and 12.8%, respectively. The blue dashed box indicates the SiPM devices used in the 8×8 SiPM array.

Propagation delay

In this detector array, the column and row signals were projected into a single side. Therefore, there is a difference in the electric signal transmission path lengths, which run from the output pin of each SiPM to the input pin of each amplifier. The path length difference among the SiPM channels resulted in a propagation delay (a trigger time difference relative to the closest channel to the amplifier). Figure 2.12 shows the propagation delay among the SiPM channels located along the 4th column of a typical SiPM device (where channel number 13 was the closest channel). From the slope of the plot in Figure 2.12, we were able to calculate a constant propagation delay of ~111 ps per SiPM channel, which would be useful information when compensating for the related TOF estimation error.

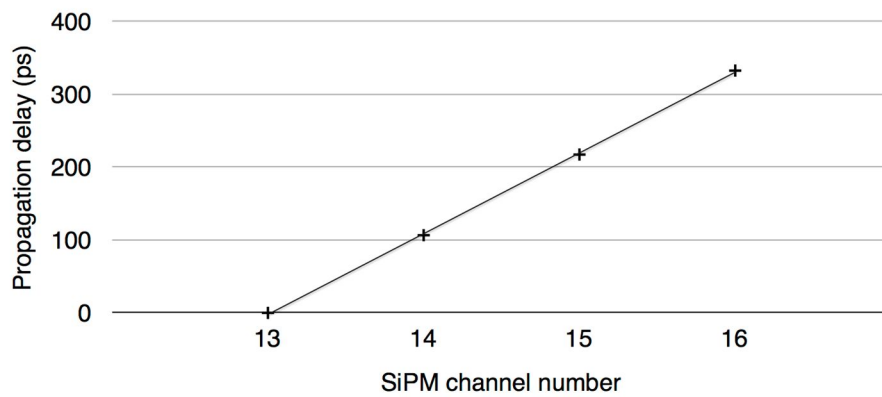


Figure 2.12 Propagation delay along the SiPM channels in a typical SiPM device. The SiPM channel number 13 was the closest channel to the input pin of the amplifier.

Multi-channel digital TDC implemented on FPGA

The multi-channel digital TDC was developed on VIRTEX-6 FPGA board. Global coarse counter measured the event time of 2-ns step via stable clock distributor in VIRTEX-6. Tapped delay line method was used to develop each channel of digital TDC. Because this method used physical unit delay, careful place and route were required. The place and route were performed using Xilinx Design Suite 13.4.

Figure 2.13 shows the delayed time of a digital TDC channel as a function of digital TDC fine counter bin using place and route simulation. In Figure 2.13, circle mark represents simulation output and the straight line represents a linear fit of data. A digital TDC channel had a time resolution of ~ 15 ps/bin and low variations. One VIRTEX-6 FPGA module can measure timing information from more than 100 signal lines.

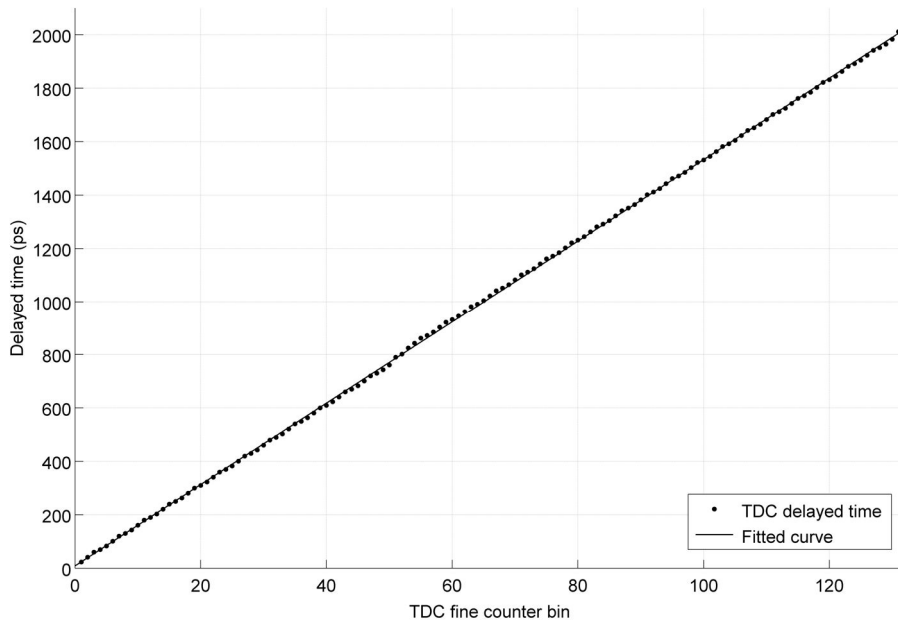


Figure 2.13 Simulation result after place and route of one channel fine counter module delay look-up-table (circle: simulated TDC delayed time, straight line: linear fit, ~ 15 ps/bin slope).

Characteristics of proposed structure

Figure 2.14 represents the dependence to the TOT value (diamond mark) on γ -ray energy obtained with a various radiation sources (^{131}I : 362 keV, ^{22}Na : 511 keV, and ^{137}Cs : 662 keV). The threshold voltages for comparators on a front-end circuit board were fixed overall measurements. Temperature controlled (20 °C) and light shielded box was used. The TOT value increased with energy of radiation source. Every radiation source was clearly distinguishable with TOT value, which was provided from proposed front-end circuit board and a digital TDC on FPGA. The photo-peak from the emitted γ -ray of ^{22}Na , which has the energy of 1.275 MeV, was also visible in TOT value distribution plot. TOT value resolutions (FWHMs) were shown in Figure 2.14 (square mark).

Time difference distributions of two proposed front-end circuit boards without SiPMs and a digital TDC on FPGA was shown in Figure 2.15. The 50-kHz square pulse with 1% duty cycle was provided to each front-end circuit board through NIM FAN OUT (N401) modules. The timing resolution between two proposed front-end circuit boards was obtained with ~ 130 ps. Timing resolutions obtained with two different transfer CAT7 cable length (1-m and 3-m) were equivalent.

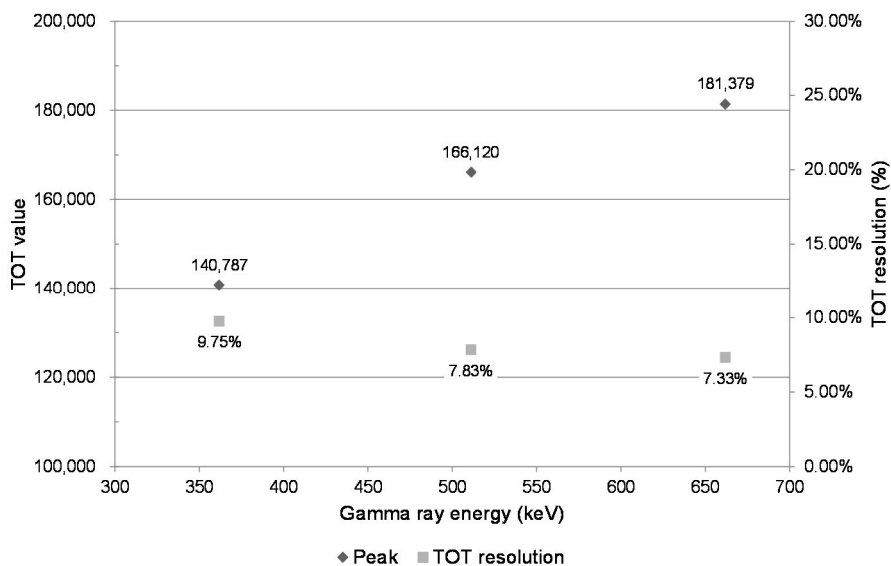


Figure 2.14 Dependences of TOT value and TOT resolution on γ -ray energy obtained with a variety of radiation sources (^{131}I : 362 keV, ^{22}Na : 511 keV, ^{137}Cs : 662 keV). The diamond and square represent TOT peak position and TOT resolution, respectively.

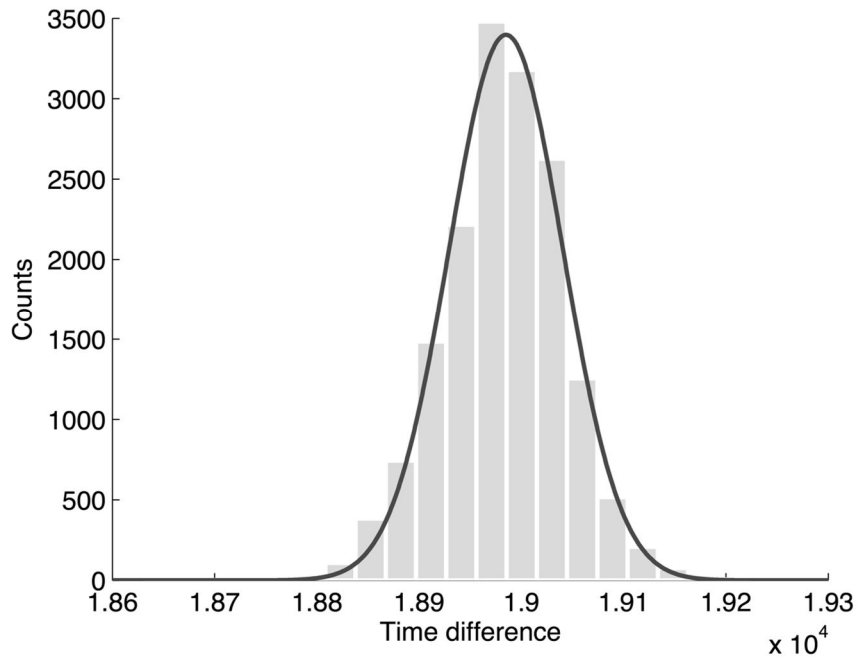


Figure 2.15 Time difference distributions of between two proposed detectors and a digital TDC on FPGA. The timing resolution between two detectors was ~ 130 ps.

Performance evaluation of proposed block detectors

Coincidence measurements using one multi-channel digital TDC on FPGA and two front-end circuit boards with SiPMs were performed with a ^{22}Na point source. Each SiPM was coupled with a $3 \times 3 \times 20 \text{ mm}^3$ LGSO crystal. A FPGA board and two front-end circuit boards were in temperature controlled ($20 \text{ }^\circ\text{C}$) and light shielded box except power supply.

Figure 2.16(a) shows TOT value spectrum plot of one proposed detector. Photo-peak region of each detector was clearly visible in TOT value spectrum with the TOT value resolution of $\sim 10\%$ FWHM. Figure 2.16(b) shows time difference distributions of coincidence measurement. The coincidence timing resolution of $\sim 450 \text{ ps}$ was obtained.

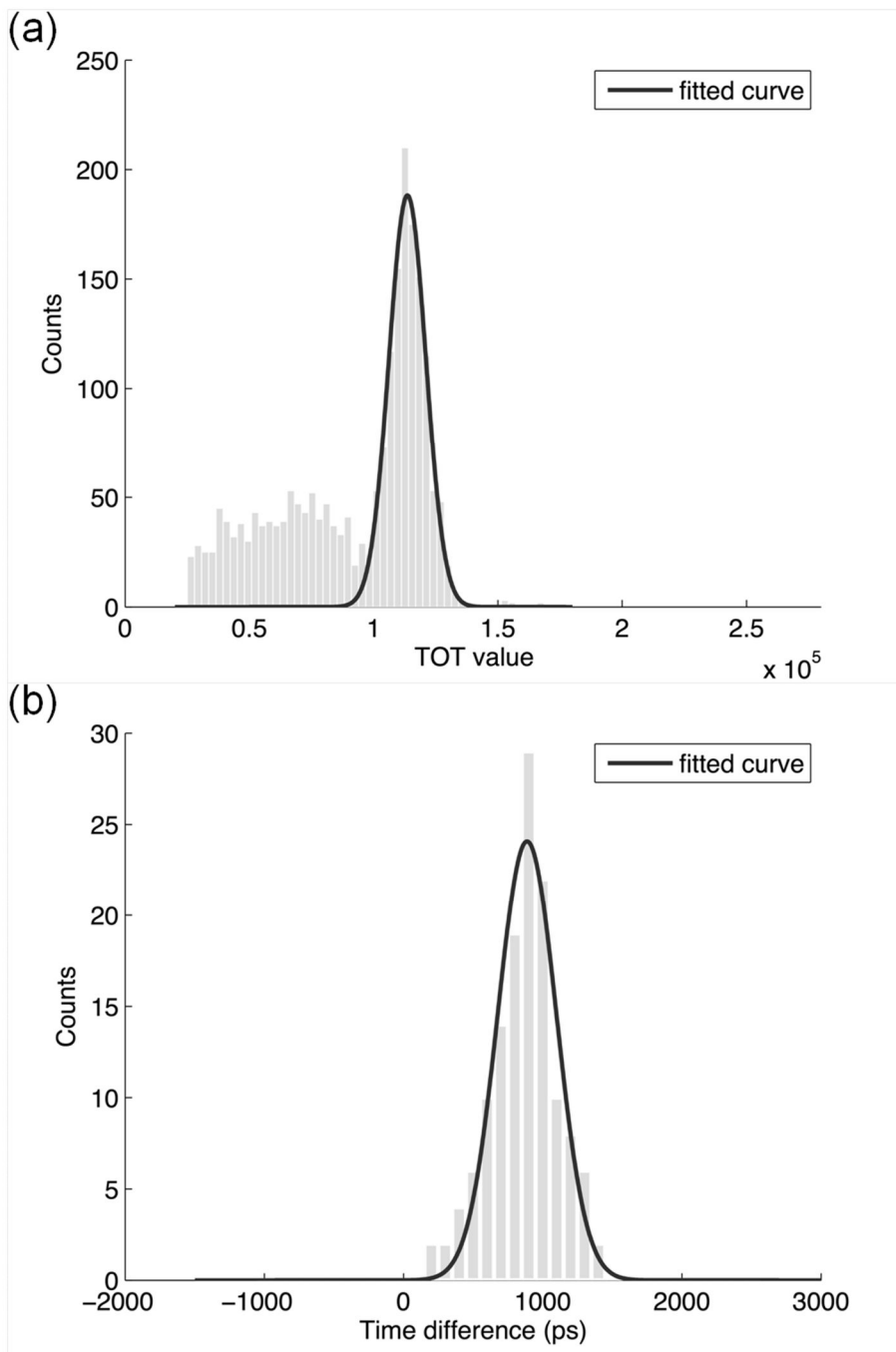


Figure 2.16 Coincidence γ -ray measurements using ^{22}Na point source and two proposed detectors; TOT value (a) and time difference (b) distributions.

DISCUSSION

In this study, we evaluated a projection-based signal encoding method for SiPM arrays in which the row and column projection signals were amplified with different gains to estimate the energy and timing information. Dedicated front-end electronics were developed and the optimal bias voltage for each SiPM was determined by considering stability in the timing resolution. For SiPM arrays with different array sizes, the timing and energy resolution were compared. The largest array size tested in this study was 12×12 , and this detector block was $\sim 5 \times 5 \text{ cm}^2$ in size, which is equivalent to the size of a block detector using 2×2 one-inch PMTs.

Most properties (i.e. the amplification gain and the dark count rate) of the SiPM output are sensitive to the bias voltage applied to the SiPM. In particular, the SiPM gain increases exponentially with increasing overvoltage, as shown in Figure 2.7. A similar gain dependence on bias voltage has also been reported for SiPM devices other than the MPPC used in this study (68, 69). In addition, the change in gain of the SiPM caused by a fractional bias change is much larger than that of the PMT. It is also known that the breakdown voltage and the bias voltage that yields the same amplification gain vary considerably across the devices (12). My results (Figure 2.8) also show that the breakdown voltage distribution across the devices is not uniform (maximum difference $\sim 2 \text{ V}$) because of the lot-to-lot variability in SiPM fabrication. In contrast, the variation of the breakdown voltage across the channels within a device was relatively small, mainly because the multi-

channel MPPC S11064-050P used in this study was produced by tiling of discrete single element MPPCs which all had similar responses. Therefore, all 16 channels in a MPPC device could be biased using a single voltage source.

In this study, it was confirmed that the SiPM coupled to a fast scintillation crystal produces excellent timing resolution, as shown in Figure 2.9. Higher overvoltage values for the SiPM lead to improved photon-detection efficiency (PDE), and improved PDE in turn results in better timing performance because of the improved photoelectron statistics at the rising edge of the output pulse (21,59). However, overvoltages higher than 2.4 V led to degradation of the timing resolution caused by an increased dark count rate, yielding the typical “U-shaped” relationship between the coincidence timing resolution and the overvoltage shown in Figure 7. Regardless of their LED thresholds, all tested MPPCs yielded this common “U-shape” relationship, with the flat region of minimal coincidence timing resolution at an overvoltage of around 2.2 V. Figure 7 also shows that the coincidence timing resolution is lowest when a 3.0% LED threshold was applied. The lower threshold is able to trigger early detection of photons, but is vulnerable to electronic noise.

The coincidence time resolution and energy resolution values of the detector modules with the various SiPM array sizes (4×4 , 8×8 , and 12×12) were measured with a 2.2 V overvoltage and a 3% LED threshold level. Detector modules containing the 4×4 array yielded consistent and good timing and energy resolution values.

As the SiPM array size increased, the average coincidence time resolution also increased. This was mainly because of the increasing number of connected column-side SiPM channels, which were used to measure the timing information. This leads to greater dark count noise for each column output in the current readout scheme. Increased count rates because of the intrinsic lutetium radioactivity of the LGSO crystal would also affect the coincidence time resolution. SiPM output pulses caused by both dark count noise and intrinsic activity have long tails (21), leading to a higher frequency of pulse pileup and baseline shift, which both have adverse effects on the timing resolution. The baseline shift is also enlarged by the other connected SiPM channels. However, the difference in coincidence timing resolution between the 4×4 and 12×12 arrays was only 24 ps.

The energy resolutions also increased slightly as the SiPM array size increased. However, this difference was also negligible.

The system performance of the PET is determined by several factors, including the spatial, timing, and energy resolutions, and the sensitivity. The crystal block used in this study does not have a sufficiently high packing fraction to yield the best γ -ray detection efficiency because we used pixelated LGSO crystals with the same front surface area ($3 \times 3 \text{ mm}^2$) as the sensitive area of each SiPM. We matched these sizes to collect as much of the scintillation light as possible. The effects of the size mismatch (a larger crystal size than the SiPM sensitive area) will be addressed in further studies, although the packing fraction of the SiPM is also improving (49.4% in the

MPPC array used in this study, but up to 74.0% in the latest version of the MPPC array).

Proposed structure, which was the combination of signals encoding method and digital TDCs on FPGA, provided energy and timing data at the same time without ADC or QDC module. Energy and timing were measured with only digital TDCs on FPGA. Based on results, time-over-threshold method using TDC was a promising alternative energy measurement method for PET scanner. In experiment results to find dependence between energy and TOT value showed, TOT value was not perfectly fitted with 1 polynomial function. More experiments with more various radioactive sources are needed to find well matched fit-function.

Intrinsic timing resolution between two developed front-end circuit boards without SiPMs using developed multi-channel TDC module was measured to estimate the influences due to the developed front-end circuit board and digital TDC. The result (~130 ps) showed that the developed front-end circuit boards and FPGA board were less affected to determine coincidence timing resolution for real coincidence measurement. However, front-end circuit board and digital TDC module should be optimized for better timing performance.

Although developed digital TDC on FPGA worked well with high timing resolution, proposed structure required a lot of digital TDC channel to make full ring system. Therefore, two or more FPGA board for multi-channel digital TDC might be connected with each other. In the next development,

FPGA board will have the synchronize module, which keep the global clock with same phase from other FPGA boards, for full ring PET scanner.

CONCLUSION

The SiPM TOF PET block detector was well designed. Coincidence timing resolution slightly increased in large array using signal encoding method. Nevertheless the resolution was still sufficient for TOF PET scanners. Multi-channel digital TDC was well developed with good LSB and intrinsic timing resolution. Energy and timing information were successfully obtained only using developed digital TDCs. The coincidence timing resolution using proposed structure showed better results than resolutions of the commercial TOF PET scanners.

Based on these results, the proposed block detector can enable the development of a simple and cost-effective TOF PET detector without individual SiPM readout of signal.

GENERAL CONCLUSION

SiPM showed stable and sufficient characteristics for the use of PET photo-sensor. SiPM block detectors for small animal PET were developed using small size of LGSO crystals. All individual LGSO crystals coupled with SiPMs were clearly distinguishable in flood images, resulting in the energy resolution for individual crystals of $25.8 \pm 2.6\%$ on average for 511 keV photo-peaks. A typical detector pair yielded an intrinsic resolution of 1.30 mm.

A Small animal PET was developed using SiPM block detectors. The reconstructed image spatial resolution measured with the ^{22}Na point source was 1.0 mm (2 mm off center) and 1.4 mm (16 mm off center) with the MLEM reconstruction algorithm. A myocardial ^{18}F -FDG study in mice and a skeletal ^{18}F study in rats demonstrated the fine spatial resolution.

A signal encoding method for a TOF PET block detector using SiPMs has been developed to reduce the complexity and volume of the signal readout and processing electronics required. The proposed encoding method showed promising results, which were measured for various SiPM array sizes. Multi-channel digital TDC was well developed with good LSB and intrinsic timing resolution. Energy and timing information were successfully obtained only using TDCs. The coincidence timing resolution using proposed structure showed better results than resolutions of the commercial TOF PET scanners.

The results obtained in this thesis indicate that SiPM is a promising photo-sensor in not only a high resolution PET scanner but also TOF PET scanner.

REFERENCES

1. Pichler BJ, Wehrl HF, Judenhofer MS. Technical advances in molecular imaging instrumentation. *J Nucl Med.* 2008;49(Suppl 2):5-23.
2. Lecomte R. Novel detector technology for clinical PET. *Eur J Nucl Med Mol Imaging.* 2009;36(Suppl 1):69-85.
3. Ziegler SI, Pichler BJ, Boening G, et al. A prototype high-resolution animal positron tomograph with avalanche photodiode arrays and LSO crystals. *Eur J Nucl Med.* 2001;28(2):136-143.
4. Abreu MC, Aguiar D, Albuquerque E, et al. Clear-PEM: A PET imaging system dedicated to breast cancer diagnostics. *Nucl Instrum Meth A.* 2007;571(1-2):81-84.
5. Fontaine R, Belanger F, Viscogliosi N, et al. The hardware and signal processing architecture of LabPET (TM), a small animal APD-based digital PET scanner. *IEEE T Nucl Sci.* 2009;56(1):3-9.
6. Pichler BJ, Judenhofer MS, Catana C, et al. Performance test of an LSO-APD detector in a 7-T MRI scanner for simultaneous PET/MRI. *J Nucl Med.* 2006;47(4):639-647.
7. Catana C, Wu Y, Judenhofer MS, Qi J, Pichler BJ, Cherry SR. Simultaneous acquisition of multislice PET and MR images: initial results with a MR-compatible PET scanner. *J Nucl Med.* 2006;47(12):1968-1976.

8. Woody C, Schlyer D, Vaska P, et al. Preliminary studies of a simultaneous PET/MRI scanner based on the RatCAP small animal tomograph. *Nucl Instrum Meth A*. 2007;571(1-2):102-105.
9. Schlemmer HP, Pichler BJ, Schmand M, et al. Simultaneous MR/PET imaging of the human brain: feasibility study. *Radiology*. 2008;248(3):1028-1035.
10. Lewellen TK. Recent developments in PET detector technology. *Phys Med Biol*. 2008;53(17):287-317.
11. Del Guerra A, Belcari N, Bisogni MG, Llosa G, Marcatili S, Moehrs S. Advances in position-sensitive photodetectors for PET applications. *Nucl Instrum Meth A*. 2009;604(1-2):319-322.
12. Lee JS, Hong SJ, Geiger-mode avalanche photodiodes for PET/MRI. In: Iniewski K, eds. *Electronic Circuits for Radiation Detection*. CRC Press LLC; 2010:179-200.
13. Saveliev V. The recent development and study of silicon photomultiplier. *Nucl Instrum Meth A*. 2004;535(1-2):528-532.
14. Renker D, Lorenz E. Advances in solid state photon detectors. *J Inst*. 2009;4: P04004.
15. Otte AN, Barral J, Dolgoshein B, et al. A test of silicon photomultipliers as readout for PET. *Nucl Instrum Meth A*. 2005;545(3):705-715.
16. Lee JS, Ito M, Sim KS, et al. Investigation of solid-state photomultipliers for positron emission tomography scanners. *J Korean Phys Soc*. 2007;50(5):1332-1339.

17. Spanoudaki VC, Mann AB, Otte AN, et al. Use of single photon counting detector arrays in combined PET/MR: Characterization of LYSO-SiPM detector modules and comparison with a LSO-APD detector. *J Inst.* 2007;2:P12002.
18. Hong SJ, Song IC, Ito M, et al. An investigation into the use of geiger-mode solid-state photomultipliers for simultaneous PET and MRI acquisition. *IEEE T Nucl Sci.* 2008;55(3):882-888.
19. Hong SJ, Kim CM, Cho SM, et al. A feasibility study on the use of optical fibers for the transfer of scintillation light to silicon photomultipliers (SiPM) for PET/MRI. *IEEE T Nucl Sci.* 2011;58(3):579-589.
20. Vinke R, Lohner H, Schaart DR, et al. Optimizing the timing resolution of SiPM sensors for use in TOF-PET detectors. *Nucl Instrum Meth A.* 2009;610(1):188-191.
21. Kim CL, Wang GC, Dolinsky S. Multi-pixel photon counters for TOF PET detector and its challenges. *IEEE T Nucl Sci.* 2009;56(5):2580-2585.
22. Lewellen TK, MacDonald LR, Miyaoka RS, McDougald W, Champley K. New directions for dMiCE - a depth-of-interaction detector design for PET scanners. *IEEE Nucl Sci Symp Conf Rec.* 2007:3798-3802
23. Shao YP, Li HR, Gao KK. Initial experimental studies of using solid-state photomultiplier for PET applications. *Nucl Instrum Meth A.* 2007;580(2):944-950.

24. Schaart DR, van Dam HT, Seifert S, et al. A novel, SiPM-array-based, monolithic scintillator detector for PET. *Phys Med Biol*. 2009;54(11):3501-3512.
25. Hong SJ, Kwon SI, Ito M, et al. Concept verification of three-layer DOI detectors for small animal PET. *IEEE T Nucl Sci*. 2008;55(3):912-917.
26. Kwon SI, Hong SJ, Ito M, et al. Development of position encoding circuit for a multi-anode position sensitive photomultiplier tube. *Nucl Med Mol Imaging*. 2008;42:469-477.
27. Miyaoka RS, Kohlmyer SG, Lewellen TK. Performance characteristics of micro crystal element (MiCE) detectors. *IEEE T Nucl Sci*. 2001;48(4):1403-1407.
28. Ito M, Lee JS, Kwon SI, et al. A four-layer DOI detector with a relative offset for use in an animal PET system. *IEEE T Nucl Sci*. 2010;57(3):976-981.
29. Ko GB, Yoon HS, Kwon SI, Hong SJ, Lee DS, Lee JS. Development of FPGA-based coincidence units with veto function. *Biomed Eng Lett*. 2011;1:27-31.
30. Wang Y, Seidel J, Tsui BM, Vaquero JJ, Pomper MG. Performance evaluation of the GE healthcare eXplore VISTA dual-ring small-animal PET scanner. *J Nucl Med*. 2006;47(11):1891-1900.
31. Tai C, Chatziioannou A, Siegel S, et al. Performance evaluation of the microPET P4: a PET system dedicated to animal imaging. *Phys Med Biol*. 2001;46(7):1845-1862.

32. National Electrical Manufacturers Association. *NEMA Standards Publication NU 4-2008: Performance Measurements of Small Animal Positron Emission Tomographs*. Rosslyn, VA: National Electrical Manufacturers Association; 2008.
33. Kim JS, Lee JS, Im KC, et al. Performance measurement of the microPET focus 120 scanner. *J Nucl Med*. 2007;48(9):1527-1535.
34. Jeong JM, Hong MK, Chang YS, et al. Preparation of a promising angiogenesis PET imaging agent: ⁶⁸Ga-labeled c(RGDyK)-isothiocyanatobenzyl-1,4,7-triazacyclononane-1,4,7-triacetic acid and feasibility studies in mice. *J Nucl Med*. 2008;49(5):830-836.
35. Lee JS, Park KS, Lee DS, Lee CW, Chung JK, Lee MC. Development and applications of a software for Functional image registration (FIRE). *Comput Meth Prog Bio*. 2005;78(2):157-164.
36. Daube-Witherspoon ME, Muehllehner G. Treatment of axial data in three-dimensional PET. *J Nucl Med*. 1987;28(11):1717-1724.
37. Yamaya T, Hagiwara N, Obi T, et al. Preliminary resolution performance of the prototype system for a 4-layer DOI-PET scanner: jPET-D4. *IEEE T Nucl Sci*. 2006;53(3):1123-1128.
38. Stapels CJ, Lawrence WG, Augustine FL, Christian JF. Characterization of a CMOS geiger photodiode pixel. *IEEE T Electron Dev*. 2006;53(4):631-635.
39. Cho G. Gamma-ray detectors for nuclear medical imaging instruments. *Nucl Med Mol Imaging*. 2008;42(2):88-97.
40. Badawi RD, Kohlmyer SG, Harrison RL, Vannoy SD, Lewellen TK.

The effect of camera geometry on singles flux, scatter fraction and trues and randoms sensitivity for cylindrical 3D PET - A simulation study. *IEEE T Nucl Sci.* 2000;47(3):1228-1232.

41. Eriksson L, Townsend D, Conti M, et al. An investigation of sensitivity limits in PET scanners. *Nucl Instrum Meth A.* 2007;580(2):836-842.
42. Lee JS. Technical advances in current PET and hybrid imaging systems. *Open Nucl Med J.* 2010. 2010;2:192–208.
43. Degenhardt C, Prescher G, Frach T, et al. The digital silicon photomultiplier — a novel sensor for the detection of scintillation light. *IEEE Nucl Sci Symp Conf Rec.* 2009:2383-2386
44. Knoess C, Siegel S, Smith A, et al. Performance evaluation of the microPET R4 PET scanner for rodents. *Eur J Nucl Med Mol Imaging.* 2003;30(5):737-747.
45. Ito M, Hong SJ, Lee JS. Positron emission tomography (PET) detectors with depth-of-interaction (DOI) capability. *Biomed Eng Lett.* 2011;1(2):70-81.
46. Ito M, Lee JS, Park MJ, Sim KS, Hong SJ. Design and simulation of a novel method for determining depth-of-interaction in a PET scintillation crystal array using a single-ended readout by a multi-anode PMT. *Phys Med Biol.* 2010;55(13):3827-3841.
47. Bao Q, Newport D, Chen M, Stout DB, Chatziioannou AF. Performance evaluation of the Inveon dedicated PET preclinical tomograph based on the NEMA NU-4 standards. *J Nucl Med.*

- 2009;50(3):401-408.
48. Ito M, Lee JP, Lee JS. Timing Performance Study of New Fast PMTs with LYSO for Time-of-flight PET. *IEEE T Nucl Sci.* [submitted]
 49. Kim CL, McDaniel DL, Ganin A. Time-of-Flight PET Detector Based on Multi-Pixel Photon Counter and Its Challenges. *IEEE T Nucl Sci.* 2011;58(1):3-8
 50. Moses WW. Time of flight in PET revisited. *IEEE Trans Nucl Sci.* 2003;50(5):1325-1330.
 51. Karp JS, Surti S, Daube-Witherspoon ME, Muehllehner G. Benefit of time-of-flight in PET: experimental and clinical results. *J Nucl Med.* 2008;49(3):462-470.
 52. Conti M. State of the art and challenges of time-of-flight PET. *Phys Med.* 2009;25(1):1-11.
 53. Crespo P, Shakirin G, Fiedler F, Enghardt W, Wagner A. Direct time-of-flight for quantitative, real-time in-beam PET: a concept and feasibility study. *Phys Med Biol.* 2007;52(23):6795.
 54. Vandenberghe S, Lemahieu I. System characteristics of simulated limited angle TOF PET. *Nucl Instrum Meth A.* 2007;571(1-2):480-483.
 55. Surti S, Karp JS. Design considerations for a limited angle, dedicated breast, TOF PET scanner. *Phys Med Biol.* 2008;53(11):2911.
 56. Moriya T, Omura T, Watanabe M, Yamashita T. Development of a position-sensitive detector for TOF-PET. *IEEE Trans Nucl Sci.* 2008;55(5):2455-2459.

57. Lee JP, Ito M, Lee JS. Evaluation of a fast photomultiplier tube for time-of-flight PET. *Biomed Eng Lett.* 2011;1(3):174-179.
58. Ito M, Lee JP, Lee JS. Timing performance study of new fast PMTs with LYSO for time-of-flight PET. *IEEE Trans Nucl Sci.* 2012:[Epub ahead of print].
59. Roncali E, Cherry SR. Application of silicon photomultipliers to positron emission tomography. *Ann Biomed Eng.* 2011;39(4):1358-1377.
60. Armin K, Eckart L, Martin SJ, Dieter R, Konrad L, Bernd JP. Evaluation of Geiger-mode APDs for PET block detector designs. *Phys Med Biol.* 2010;55(7):1815.
61. Hong SJ, Kang HG, Ko GB, Song IC, Rhee J-T, Lee JS. SiPM-PET with a short optical fiber bundle for simultaneous PET-MR imaging. *Phys Med Biol.* 2012;57(12):3869.
62. Yoon HS, Ko GB, Kwon SI, et al. Initial results of simultaneous PET/MRI experiments with an MRI-compatible silicon photomultiplier PET scanner. *J Nucl Med.* 2012;53(4):608-614.
63. Ko GB, Yoon HS, Kwon SI, et al. Development of a front-end analog circuit for multi-channel SiPM readout and performance verification for various PET detector designs. *Nucl Instrum Meth A.* 2013;703(0):38-44.

64. Seiichi Y, Masao I, Tadashi W, et al. Development of a Si-PM-based high-resolution PET system for small animals. *Phys Med Biol.* 2010;55(19):5817.
65. Schaart DR, Seifert S, Vinke R, et al. LaBr(3):Ce and SiPMs for time-of-flight PET: achieving 100 ps coincidence resolving time. *Phys Med Biol.* 2010;55(7):179-189.
66. Popov V, Majewski S, Weisenberger AG. Readout electronics for multianode photomultiplier tubes with pad matrix anode layout. *Nuclear Science Symposium Conference Record, 2008 NSS '08 IEEE.* 19-25 Oct. 2003 2003;3:2156-2159.
67. Seiichi Y, Hiroshi W, Jun H. Performance comparison of Si-PM-based block detectors with different pixel sizes for an ultrahigh-resolution small-animal PET system. *Phys Med Biol.* 2011;56(20):227-236.
68. Musienko Y, Reucroft S, Swain J. Tests and performance of multi-pixel Geiger mode APD's. *Int. Workshop on New Photon-detectors.* Kobe, Japan; 2007.
69. Ramilli M. Characterization of SiPM: Temperature dependencies. *Nuclear Science Symposium Conference Record, 2008 NSS '08 IEEE.* 2008:2467-2470.

초록

실리콘광증폭기를 이용한 PET 검출기 개발

권순일
서울대학교 의과대학
협동과정 방사선응용생명과학

실리콘광증폭기(Silicon photomultiplier; SiPM)은 반도체 광전 소자로서 양전자 단층촬영장치 (Position emission tomography; PET)에서 기존에 사용되었던 광전증배관(photomultiplier tube; PMT)를 대체할 수 있는 광전소자로 주목 받고 있다. 광전증배관과 유사한 신호 이득을 가지며 빠른 신호 상승시간으로 입사되는 감마선의 시간을 정밀히 측정할 수 있는 기반을 제공한다. 또한 자기장의 영향을 적게 받아 기능성 영상을 제공하는 PET 과 해부학적 영상을 제공하는 MRI 영상을 동시에 획득 할 수 있는 동시계측 PET/MRI 개발에 사용될 수 있다. 본 연구에서는 SiPM 소자를 사용하여 소동물용 PET 검출기 및 시스템 개발을 통해 SiPM 이 PET 검출기에 사용될 수 있는지를 확인하고 나아가 SiPM 의 빠른 상승 시간을 이용한 임상용 시간차 측정 PET 검출기를 개발하여 SiPM 소자의 활용범위를 제시하고자 한다.

초기에 개발된 단일 채널 SiPM 소자를 사용하여 소동물용 SiPM PET 을 개발하였다. 개발된 소동물용 PET 은 8 개의 블록

검출기로 구성되어 있다. 각 검출기는 12 개의 단일 채널 SiPM 소자가 2×6 형태로 배열되어 4×13 개의 LGSO 섬광결정 ($1.5 \times 1.5 \times 7 \text{ mm}^3$)으로부터 감마선을 검출한다. 내측 직경은 6.0 cm 이고 종축 시야는 6.5 mm 로 마우스(mouse)의 전신이나 랫(rat)의 PET 영상 획득이 가능하다. SiPM 소자의 전압 이득율은 소자에 가해진 바이어스 전압에 매우 민감하게 반응하기 때문에 디지털로 조정되는 전압회로가 각각의 SiPM 소자에 공급되었다. 개발된 소동물용 PET 의 성능 평가를 위해 ^{22}Na 점선원을 사용하여 성능평가를 수행하였고, 팬텀, 마우스 및 랫의 PET 영상을 획득하였다. 모든 검출기의 섬광결정이 명확하게 구분되었고, 에너지 분해능은 $25.8 \pm 2.6\%$ 이었다. 점선원을 사용한 공간분해능 측정 결과 중심에서 2 mm 떨어진 위치에서 1.0 mm, 16 mm 떨어진 곳에서 1.4 mm 의 공간 분해능을 보였다. 이때 MLEM 재구성 알고리즘이 적용되었다. ^{18}F -FDG 및 ^{18}F 을 주사한 마우스와 랫의 영상을 획득하였고 기존 광전증배관을 사용한 소동물용 PET 과 비교할만한 결과를 획득하였다.

SiPM 소자의 빠른 시간 특성을 이용하여 검출 시간차 측정이 가능한 임상용 time-of-flight (TOF) PET 검출기를 개발하였다. 증가되는 신호 선 및 회로면적을 최적화 하기 위하여 새로운 신호선 축소 기법 및 측정 방법을 제시하였다. 개발된 임상용 검출기는 신호선 축소 기법이 적용된 $M \times N$ 의 SiPM 배열로

구성된 전단 회로부와 FPGA 에 신호측정을 할 수 있는 디지털신호 계측기를 구현한 보드로 구성된다. 각각의 SiPM 광전소자들은 LGSO ($3 \times 3 \times 20 \text{ mm}^3$) 섬광결정과 일대 일로 접합되어 있다. 신호선 축소 기법은 각각의 SiPM 출력신호를 개별적으로 열과 행으로 나누어 해당되는 열과 행의 다른 소자의 출력과 결합하여 신호를 축소한다. 본 기법을 사용할 경우 신호선의 수를 $M \times N$ 에서 $M + N$ 으로 줄일 수 있다. 수집된 열과 행의 신호는 각각 에너지와 시간 정보를 획득하는데 사용된다. 축소된 신호선들은 디지털 신호 계측기가 구현된 FPGA 에 연결되고, 입사된 열과 행의 신호들은 시간측정을 통해 각각 에너지와 입사시간을 측정에 사용되었다. 에너지를 시간정보로 획득하기 위하여 time over threshold 방법으로 에너지를 획득하였다.

신호선 축소 기법을 검증하기 위해 4×4 , 8×8 , 12×12 의 SiPM 배열을 사용하여 성능을 비교하였다. FPGA 에 디지털 신호 계측기를 구현하고 4×4 SiPM 배열과 결합하여 전체 구성을 완료하고 특성을 측정하였다. 신호선 축소 기법을 통해 성능을 평가한 결과 12×12 의 배열크기에서도 TOF PET 구현이 가능한 우수한 시간분해능을 획득하였다. VIRTEX-6 FPGA 에 구현된 디지털 신호 계측기는 최소 비트 $\sim 15 \text{ ps}$ 를 갖도록 구현되었다. 또한 개발된 신호보드와 결합하여 고유의 시간분해능은 $\sim 130 \text{ ps}$ 로 측정되었다. 개발된 디지털 시간

계측기를 통해 세 개의 서로 다른 에너지를 가지는 점선원의 에너지를 측정하였고 서로 다른 에너지로 구분되어 가능성이 검증되었다. 개발된 검출기 구성으로 ^{22}Na 점선원을 사용하여 동시 감마선을 측정한 결과 ~ 450 ps 의 시간 분해능을 획득하였다.

결론적으로 실리콘 광전소자인 SiPM은 전임상 및 임상에서 사용할 수 있는 PET 개발에 적합하였으며, 우수한 시간 분해능을 획득함으로써 시간 차이 측정이 가능한 PET 검출기로 사용될 수 있을 것이다.

주요어: PET, 실리콘 광전소자 (SiPM), PET/MR, time-of-flight PET, time-over-threshold, time-to-digital converter

학번: 2007-22070